

Spurious heating of stellar motions by dark matter particles in cosmological simulations of galaxy formation

Aaron D. Ludlow^{1,*}, S. Michael Fall², Matthew J. Wilkinson¹, Joop Schaye³, Danail Obreschkow¹

¹International Centre for Radio Astronomy Research, University of Western Australia, 35 Stirling Highway, Crawley, Western Australia, 6009, Australia

²Department of Physics and Astronomy, Johns Hopkins University, 3400 N. Charles St., Baltimore, MD, 21218, USA

³Leiden Observatory, Leiden University, PO Box 9513, 2300 RA Leiden, the Netherlands

Accepted XXX. Received YYY; in original form ZZZ

ABSTRACT

We use two cosmological simulations to study the impact of spurious heating of stellar motions within simulated galaxies by dark matter (DM) particles. The simulations share the same numerical and subgrid parameters, but one used a factor of 7 more DM particles. Many galaxy properties are unaffected by spurious heating, including their masses, star formation histories, and the spatial distribution of their gaseous baryons. The distribution and kinematics of stellar and DM particles, however, are affected. Below a resolution-dependent virial mass, M_{200}^{spur} , galaxies have higher characteristic velocities, larger sizes, and more angular momentum in the simulation with lower DM mass resolution; haloes have higher central densities and lower velocity dispersions. Above M_{200}^{spur} , galaxies and haloes have similar properties in both runs. The differences arise due to spurious heating, which transfers energy from DM to stellar particles, causing galaxies to heat up and haloes to cool down. The value of M_{200}^{spur} can be derived from an empirical disc heating model, and coincides with the mass below which the predicted *spurious* velocity dispersion exceeds the *measured* velocity dispersion of simulated galaxies. We predict that galaxies in the 100^3 Mpc^3 EAGLE run and IllustrisTNG-100 are robust to spurious collisional effects at their half-mass radii provided $M_{200}^{\text{spur}} \approx 10^{11.7} M_{\odot}$; for the 25^3 Mpc^3 EAGLE run and IllustrisTNG-50, we predict $M_{200}^{\text{spur}} \approx 10^{11} M_{\odot}$. Suppressing spurious heating at smaller/larger radii, or for older/younger stellar populations, requires haloes to be resolved with more/fewer DM particles.

Key words: galaxies: kinematics and dynamics – galaxies: formation – galaxies: evolution – galaxies: structure – galaxies: haloes – methods: numerical

1 INTRODUCTION

Relaxation driven by scattering between stars or dark matter (DM) particles is believed to be negligible for most galaxies. Simulations of galaxy formation aim to emulate this collisionless behaviour, and although they continue to improve, most do not model individual systems with particle numbers that are even close to the number of stars, let alone DM particles, in real galaxies; they instead employ fewer, more massive ones. Simulated galaxies and their DM haloes are therefore susceptible to spurious evolution due to the finite number of particles with which they are resolved, which gives rise to incoherent fluctuations in their gravitational potential that deflect individual particle trajectories (e.g. Lacey & Ostriker 1985; Hernquist & Barnes 1990; Sellwood 2013, 2015). This gravitational scattering process (that we refer to as “spurious heating”) can be detrimental to the structure and kinematics of simulated galaxies.

Using a suite of idealised simulations of isolated galactic discs, Ludlow et al. (2021) and Wilkinson et al. (2023) showed that spurious heating randomises the orbits of stellar particles, thus increasing

the velocity dispersion and thickness of discs, and affecting the locations of galaxies on a number of fundamental scaling relations. They provided a simple empirical model that quantifies the effects of spurious heating on the velocity dispersion and scale heights of stellar disc particles. For simulations that adopt DM particle masses of $m_{\text{DM}} \gtrsim 10^6 M_{\odot}$, such as EAGLE (Schaye et al. 2015; Crain et al. 2015) and IllustrisTNG-100 (Pillepich et al. 2018), their model predicts that spurious heating can be significant in haloes with masses below about $10^{12} M_{\odot}$, suggesting that many galaxies of interest in large-volume cosmological simulations will suffer ill effects.

Although spurious heating is critically important for simulations of idealised galactic discs, the consequences for galaxies in cosmological simulations is less clear. Idealised simulations, for example, neglect a variety of important physical processes that also give rise to disk heating: the scattering of stellar orbits by spiral arms, globular clusters, or giant molecular clouds, for example, or dynamical heating driven by accretion or close encounters with nearby satellite galaxies. Idealised simulations also conserve mass and typically disregard the time-dependent growth of the DM halo as well as the formation of new stars in a thin, rotationally supported disk. When

* E-mail: aaron.ludlow@icrar.org

acting in concert, these processes will either exacerbate or mitigate the effects of spurious heating in cosmological runs.

Spurious heating, however, *is present* in cosmological simulations of galaxy formation. Ludlow et al. (2019a, see also Revaz & Jablonka 2018) showed that galaxies in the intermediate resolution EAGLE simulation (for which $m_{\text{DM}} = 9.7 \times 10^6 M_{\odot}$) with stellar masses $M_{\star} \lesssim 10^{10} M_{\odot}$ are subject to spurious size growth due to collisional heating. But what other galaxy properties inferred from cosmological simulations are affected by spurious heating? Do the insights obtained from idealised simulations apply to galaxies formed in cosmological ones? And how, if at all, can we distinguish spurious results from robust ones? This paper addresses these questions.

Our paper is structured as follows. In Section 2 we describe our simulations and analysis techniques. Our main results are presented in Section 3, where we highlight several galaxy properties that *are not* affected by spurious heating; and in Section 4, where we identify and compare properties of galaxies that *are* affected by spurious heating. In Section 5 we discuss the implications of our results for resolving the inner regions of galaxies and haloes, and provide a simple convergence criterion that can be used to separate galaxies whose properties are robust to spurious heating from those whose properties are not. We summarise our results in Section 6.

2 NUMERICAL SIMULATIONS AND ANALYSIS

2.1 The simulations

We analyse the $z = 0$ outputs of two cosmological simulations of galaxy formation that differ only in the resolution of their DM components, but keep the baryon mass resolution, force softening, and subgrid physics fixed. One simulation is Ref – L050N0752 of the EAGLE project (see Table 2 of Schaye et al. 2015), which follows the evolution of cosmic structure in a comoving cube with edge lengths $L_{\text{box}} = 50 \text{ Mpc}$ initially using $N_{\text{DM}} = N_{\text{gas}} = 752^3$ particles of both DM and baryons. The second simulation uses the same box size and number of baryonic particles, but to study the effects of higher DM mass resolution we split each DM particle equally into 7 lower-mass ones. Throughout the paper we refer to these runs as LoResDM and HiResDM, respectively.¹

Both simulations were run with the same version of GADGET3 (Springel 2005; Schaye et al. 2015) that was used for EAGLE, and employed the same numerical parameters for hydrodynamics and gravitational force integration. We adopted the “Reference” subgrid models and parameters for cooling and star formation, and for feedback from stars and active galactic nuclei (see Schaye et al. 2015, for details); the parameters were not recalibrated for HiResDM to accommodate any effects of its higher DM mass resolution.

We adopt cosmological parameters advocated by the Planck Collaboration et al. (2014). The initial² baryonic particle mass is therefore $m_{\text{gas}} = 1.81 \times 10^6 M_{\odot}$ for both runs, and the DM particle

masses are $m_{\text{DM}} = 9.70 \times 10^6 M_{\odot}$ for LoResDM³ and $m_{\text{DM}} = 1.39 \times 10^6 M_{\odot}$ for HiResDM. We will sometimes quote the DM-to-baryonic particle mass ratio, i.e. $\mu \equiv m_{\text{DM}}/m_{\text{gas}}$, which is initially $\mu \approx 5.36$ for LoResDM and ≈ 0.77 for HiResDM.

The gravitational softening lengths are the same for both runs for all particle species; they were chosen to be a fixed fraction of the Lagrangian baryonic inter-particle separation, $l_{\text{bar}} = L_{\text{box}}/N_{\text{gas}}^{1/3}$. For redshifts $z > 2.8$ the value is $\varepsilon/l_{\text{bar}} = 0.04$ in comoving units and at lower redshifts it is $\varepsilon/l_{\text{bar}} = 0.011$ in physical units; at $z \leq 2.8$, this corresponds to a physical softening length $\varepsilon = 700 \text{ pc}$. Inter-particle forces are exactly Newtonian above the *spline* softening length, $\varepsilon_{\text{sp}} = 2.8 \times \varepsilon$.

2.2 Halo identification and matching

We use SUBFIND to identify gravitationally bound DM haloes and their associated galaxies (Springel et al. 2001). SUBFIND identifies friends-of-friends (FoF) DM haloes and divides them into self-bound “subhaloes”. We refer to the most massive subhalo of each FoF group as the *central* subhalo; the rest are satellite subhaloes. SUBFIND also associates baryonic particles to each central and satellite subhalo – we refer to them as central and satellite *galaxies*, respectively. The centres of haloes, subhaloes, and galaxies coincide with their DM particle that has the lowest gravitational potential energy.

On mutually-resolved scales, both runs employed the same initial Fourier modes for density fluctuations allowing individual haloes in LoResDM to be matched to their counterparts in HiResDM. But because the total number of DM particles differ, matching haloes by their DM particle IDs is not possible. We instead adopt a different approach, as follows.

For each central halo in HiResDM at $z = 0$, we select 50 DM particles with the lowest potential energies and determine their Lagrangian coordinates in the initial conditions (ICs) of the simulation. We next locate the 50 nearest DM particles in the ICs of LoResDM, and determine the $z = 0$ halo (if any) to which the majority of them belong; we accept a halo in LoResDM as a potential match to the one in HiResDM if it contains at least 25 of them. We then repeat the procedure in reverse, using haloes in LoResDM as the starting point. We note that $\gtrsim 96$ per cent of centrals with total masses $\gtrsim 10^{10} M_{\odot}$ were bijectively matched between the two runs.

Table 1 lists some important numerical aspects of the simulations, as well as some basic properties of the halo and galaxy populations.

2.3 Analysis

We define the virial masses⁴ of central galaxies (hereafter centrals) as M_{200} . The masses of satellite haloes, M_{sub} , are defined as the sum of the masses of their gravitationally bound particles (baryonic plus dark matter). The stellar or gas mass of a central or satellite galaxy

¹ A similar pair of simulations was carried out by Richings et al. (2021) but in a smaller volume, $L_{\text{box}} = 25 \text{ Mpc}$. These were the same runs used by Ludlow et al. (2019a) to study the impact of spurious heating on simulated galaxy sizes. We refer to those papers for additional information.

² Because of star formation and mass transfer between stellar and gas particles the masses of baryonic particles may evolve with time.

³ This is the same DM particle mass that was used for the 100 cubic Mpc flagship run of the EAGLE project, referred to as L100N1504 in Table 2 of Schaye et al. (2015).

⁴ The virial mass, M_{200} , is the total mass of all particle species enclosed by a sphere of radius r_{200} (measured relative to the halo centre) that encloses a mean density equal to $200 \times \rho_{\text{crit}}(z)$, where $\rho_{\text{crit}} = 3H^2(z)/8\pi G$ is the critical density for closure at redshift z , G is the gravitational constant, and $H(z)$ is the Hubble-Lemaître parameter. The corresponding virial circular velocity is $V_{200} = (GM_{200}/r_{200})^{1/2}$.

Table 1. Numerical aspects of our simulations. From left to right: simulation name, box side length (L_{box}), the total number of dark matter particles and the initial number of baryonic particles (N_{DM} and N_{gas} , respectively), dark matter and (primordial) baryonic particle masses (m_{DM} and m_{gas} , respectively), and dark matter-to-baryonic particle mass ratio ($\mu \equiv m_{\text{DM}}/m_{\text{gas}}$). N_{cent} and N_{sub} are the total number of central haloes and satellite subhaloes, respectively, with masses greater than $100 \times m_{\text{DM}}$. Similarly, N_{gal} and N_{sat} are the number of central and satellite galaxies, respectively, with stellar masses greater than $10 \times m_{\text{gas}}$.

Sim. Name	L_{box} [Mpc]	N_{DM}	N_{gas}	m_{DM} [$10^5 M_{\odot}$]	m_{gas} [$10^5 M_{\odot}$]	μ $m_{\text{DM}}/m_{\text{gas}}$	N_{cent} $\geq 100 m_{\text{DM}}$	N_{sub} $\geq 100 m_{\text{DM}}$	N_{gal} $\geq 10 m_{\text{gas}}$	N_{sat} $\geq 10 m_{\text{gas}}$
LoResDM	50	752 ³	752 ³	97.0	18.1	5.36	70,338	22,141	7,932	5,551
HiResDM	50	7×752^3	752 ³	13.9	18.1	0.77	445,665	128,243	7,483	6,139

– M_{\star} or M_{gas} , respectively – is defined as the sum of the masses of all gravitationally bound particles of that type.⁵

In addition to masses, we also calculate a number of dynamical and structural properties of the galaxies. We adopt a coordinate system centred on each galaxy and at rest with respect to its centre-of-mass motion (defined as the mass-weighted mean velocity of its stellar particles); the z -axis is chosen to coincide with the total (stellar) angular momentum vector of the galaxy.

Galaxy sizes are quantified by their three dimensional stellar half-mass radius, r_{50} (we will use lower case “ r ” and capital “ R ” to distinguish spherical and cylindrical radii, respectively; in our coordinate system, $R^2 \equiv r^2 - z^2$).

We quantify the thickness of galactic discs using the stellar half-mass height, z_{50} , calculated in an annular aperture of central radius $R = r_{50}$ and width $\Delta \log R = 0.3$. In the same aperture we also calculate the stellar velocity dispersion, $\sigma_{\star,50}$, defined as⁶

$$\sigma_{\star,50}^2 = \frac{\sum_k m_k v_k^2}{\sum_k m_k}, \quad (1)$$

where v_k is the velocity norm of particle k in the reference frame of the galaxy, m_k is its mass, and the sums extend over all particles k in the annulus. Note that we do not subtract the mean azimuthal velocities of stellar particles; $\sigma_{\star,50}^2$ is therefore equal to twice the specific kinetic energy of stellar particles within the shell.

We construct spherically averaged circular velocity profiles due to DM, stellar, and gas particles, and define the total circular velocity profile (squared) as

$$V_c^2(r) \equiv \frac{GM_{\text{tot}}(r)}{r} = V_{\text{DM}}^2(r) + V_{\star}^2(r) + V_{\text{gas}}^2(r), \quad (2)$$

where $M_{\text{tot}}(r)$ is total enclosed mass and the subscripts indicate the matter components. Although strictly valid only for spherical systems, we use equation (2) as a proxy for the galactic rotation velocity, which we define as the total circular velocity at r_{50} : $V_{c,50} \equiv V_c(r_{50})$. When defined this way, late-type galaxies in EAGLE and IllustrisTNG-100 with $M_{\star} \gtrsim 10^{10} M_{\odot}$ follow a Tully-Fisher (1977) relation that agrees well with observations (Ferrero et al. 2017).

Scaling laws that relate the above quantities often depend on galaxy morphology. We separate galaxies by morphological type using κ_{co} , defined as the fraction of kinetic energy in stellar orbits

⁵ Several earlier studies based on EAGLE defined M_{\star} as the integrated mass of bound stellar particles contained within a fixed physical aperture, commonly 30kpc. Adopting this definition changes slightly the masses of a handful of the most massive galaxies in our runs but otherwise has no impact on our results.

⁶ In Appendix B, we also consider characteristic radii r_f that enclose different stellar mass fractions f , namely the radii r_{25} and r_{75} that enclose 25 and 75 per cent of the galactic stellar mass, respectively. The local velocity dispersion at r_f will be denoted explicitly $\sigma_{\star,f}$.

co-rotating with the galaxy⁷ (Sales et al. 2010; Correa et al. 2017). Correa & Schaye (2020) showed that, for $M_{200} \gtrsim 10^{12} M_{\odot}$, the halo mass dependence of the disc and spheroid fractions in the Sloan Digital Sky Survey (Data Release 7; York et al. 2000; Abazajian et al. 2009) are reproduced by EAGLE using the thresholds $\kappa_{\text{co}} \geq 0.35$ and $\kappa_{\text{co}} \leq 0.25$, respectively. We note, however, that more direct methods of estimating galactic morphology – based, for example, on disk-to-bulge ratios, or dynamical decomposition of galactic structures – may yield different boundaries between discs and spheroids whose structural scaling relations may differ from those presented in Section 4. We plan to study the impact of spurious heating on galactic morphology in a follow-up paper; for the present paper, we adopt the κ_{co} thresholds advocated by Correa & Schaye (2020) without further justification.

It will sometimes be necessary to distinguish a quantity measured in one of our simulations from the same quantity measured in the other. We will do so using superscripts: “HR” for HiResDM and “LR” for LoResDM. For example, the stellar mass of a galaxy in LoResDM will sometimes be denoted M_{\star}^{LR} .

3 GALAXY PROPERTIES THAT ARE NOT SIGNIFICANTLY AFFECTED BY SPURIOUS HEATING

In this section we present several important properties of the simulated galaxy population that are *not* significantly affected by spurious heating; In Section 4 we present a few properties that *are* significantly affected.

3.1 Stellar, gas, and central supermassive black hole masses of central galaxies

Fig. 1 plots the logarithmic difference between the stellar masses (top panel), gas masses (middle panel), and central black hole masses (bottom panel) of matched centrals as a function of M_{200}^{HR} , the halo virial mass in HiResDM.⁸ Green symbols show individual galaxies and the thick lines with black boundaries are the median relations. Note that all three baryonic masses are in good agreement, even down to the lowest values of M_{200}^{HR} plotted ($10^{10} M_{\odot}$).

The lightly shaded regions in each panel indicate the interquartile range (IQR). For M_{\star} and M_{gas} , the scatter decreases with increasing halo mass (although it is larger for M_{gas} than for M_{\star} at all masses).

⁷ Specifically, we adopt the definition $\kappa_{\text{co}} = (2K_{\star})^{-1} \sum_{j_{z,k} > 0} m_k (j_{z,k}/R_k)^2$, where $j_{z,k}$ is the vertical component of the specific angular momentum of particle k and K_{\star} is the total kinetic energy of the stellar particles.

⁸ We find that the virial masses of matched galaxies used in our analysis are in excellent agreement, typically within a few per cent, and with no systematic bias. Using M_{200}^{HR} , M_{200}^{LR} , or their average as the independent variable in Fig. 1 does not affect the results.

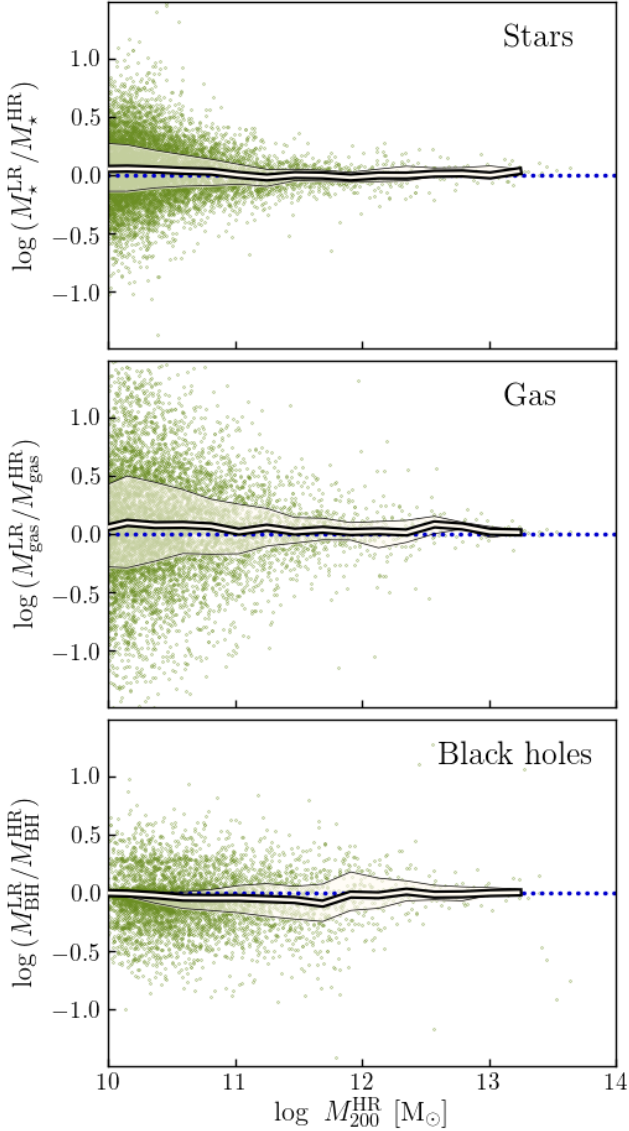


Figure 1. Logarithmic difference between the stellar (top panel), gas (middle panel), and central supermassive black hole masses (lower panel) of individual central galaxies that were matched between LoResDM and HiResDM. Results are plotted as a function of the virial mass in the HiResDM run, i.e. M_{200}^{HR} . The thick lines with black boundaries show the median relations and the lightly shaded regions indicate the interquartile scatter. Individual galaxies are plotted using green points. Each of these baryonic masses are strongly correlated, although the scatter in M_* and M_{gas} increases toward lower halo masses. For BHs, the small scatter at low halo masses is due to the majority of those galaxies hosting single BHs with masses approximately equal to their seed mass.

For example, galaxies with $M_* \geq 10^{10} M_{\odot}$ have an interquartile scatter about the one-to-one logarithmic relation of $\text{IQR} = 0.09$ for M_* and $\text{IQR} = 0.16$ for M_{gas} ; for $M_* < 10^{10} M_{\odot}$, the scatter increases to $\text{IQR} = 0.29$ for M_* and $\text{IQR} = 0.54$ for M_{gas} .

The scatter cannot be attributed to Poisson noise alone, for which the relative mass difference is expected to be $\sim 1/\sqrt{N_i}$, where N_i is the number of particles of species i . As discussed by Borrow et al. (2022), it is partially due to stochastic differences in the star formation histories of individual galaxies that arise due to the star for-

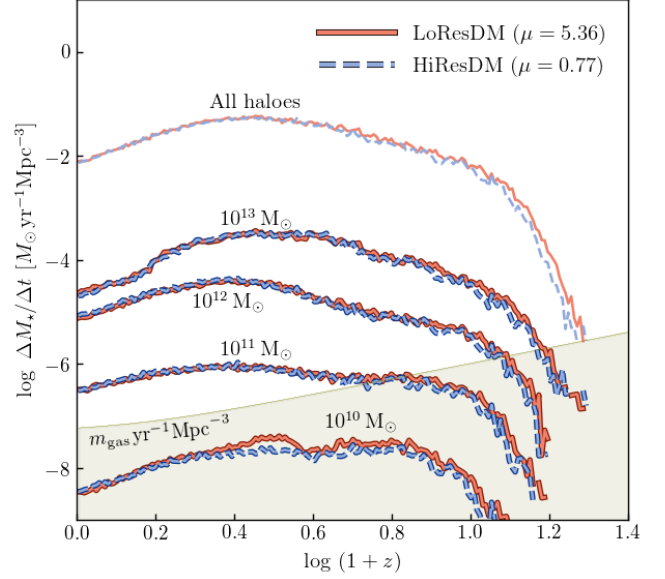


Figure 2. Average star formation histories (SFHs) for central galaxies occupying DM haloes with different $z = 0$ virial masses (the values of M_{200} are chosen to lie within ± 0.15 dex of the values indicated near each pair of curves). Results are shown for LoResDM using solid orange lines and for HiResDM using dashed blue lines. The uppermost set of curves (plotted as thin lines) show the total star formation history in each simulation. The shaded region indicates star formation rates less than $m_{\text{gas}} \text{yr}^{-1} \text{Mpc}^{-3}$. Present-day star formation rates as well as past star formation histories are, on average, unaffected by the higher DM mass resolution used for HiResDM.

mation and feedback models adopted for EAGLE (see also Genel et al. 2019; Keller et al. 2019), but the spurious collisional effects discussed in this paper may also contribute.

The mass-dependence of the scatter in BH masses differs from that for M_* and M_{gas} . In this case, the scatter about the one-to-one logarithmic relation at $M_* < 10^{10} M_{\odot}$ ($\text{IQR} = 0.02$) is considerably lower than it is at $M_* \geq 10^{10} M_{\odot}$ ($\text{IQR} = 0.13$). At sufficiently low masses, $M_{200} \lesssim 10^{10.4} M_{\odot}$, most galaxies in both runs host only one BH particle whose mass is roughly equal to the BH seed mass (i.e. $M_{\text{BH}} = 10^{5.5} M_{\odot}$) and the interquartile scatter drops to zero. The remaining scatter at these masses is due to small differences in the BH accretion rates in low-mass haloes, or because galaxies in one simulation contain central BHs that have undergone one or a few mergers with other seed-mass BHs but their counterparts in the other simulation have not.

3.2 Star formation histories and star formation rates

The strong correlation between the stellar masses of individual galaxies shown in Fig. 1 results from their similar star formation histories (SFHs). We show this explicitly in Fig. 2, where we plot the average SFHs of centrals occupying DM haloes with present-day virial masses ranging from $M_{200} = 10^{10} M_{\odot}$ to $10^{13} M_{\odot}$ (the corresponding number of DM particles within r_{200} range from $N_{200} \approx 10^3$ to $\approx 10^6$ in LoResDM, and a factor of 7 more DM particles in HiResDM); for comparison, the total star formation rate densities averaged over all haloes are shown as thin lines. Results from LoResDM are plotted using solid orange curves and those from HiResDM as dashed blue curves (a colour convention used for the majority of plots that follow).

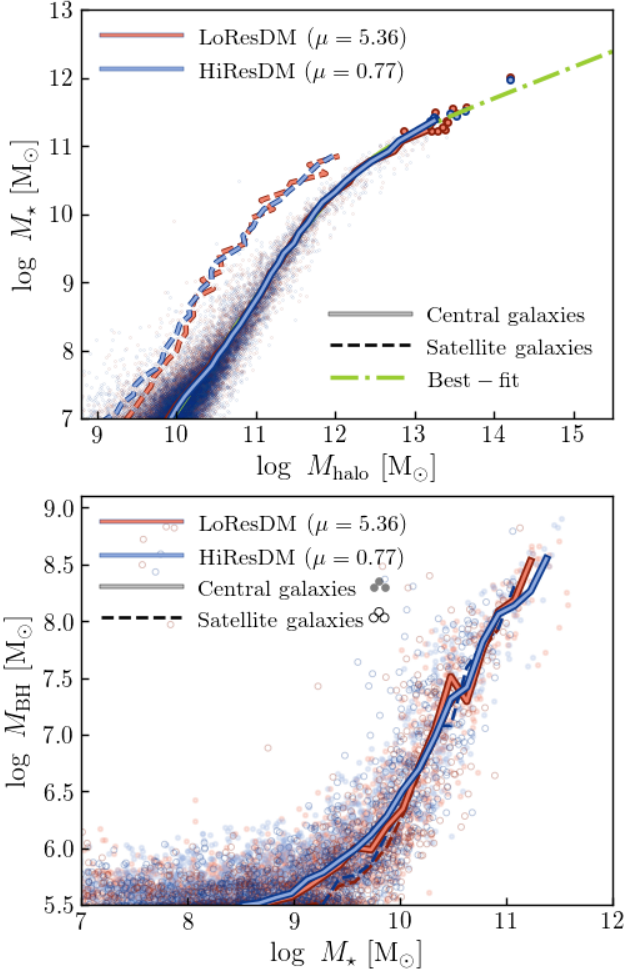


Figure 3. Upper panel: Median stellar-to-halo mass relation for central (solid lines) and satellite galaxies (dashed lines). For centrals, halo masses are defined as M_{200} ; for satellites, we use the total gravitationally bound mass, M_{sub} , identified by SUBFIND. Individual central galaxies are shown as dots, or as circles in bins populated by fewer than 10 systems. As in Fig. 2, orange lines show the median relations for LoResDM and blue lines for HiResDM. The green dashed line is the best-fitting double power-law to the $M_* - M_{\text{halo}}$ relation of centrals. Lower panel: Black hole mass-stellar mass relation for central and satellite galaxies. Median relations and individual systems are shown as solid lines and filled circles, respectively, for centrals, and as dashed lines and open circles, respectively, for satellites.

The average SFHs of galaxies are remarkably similar for LoResDM and HiResDM at all redshifts and for all $z = 0$ halo masses. This suggests that cosmic star formation is largely unaffected by spurious heating, at least for the DM particle masses and the DM-to-stellar particle mass ratios studied here (i.e. $\mu \approx 5.36$ and 0.77). Good agreement in the specific star formation rates of galaxies at redshifts $z \geq 0$ is implicit in these results.

We have verified that the mass fraction, as well as the spatial and density distribution of star forming gas particles inside individual haloes are also well-converged. Steinmetz & White (1997) showed that discreteness effects give rise to spurious heating of gas particles by DM halo particles that can counteract the effects of radiative cooling in poorly resolved haloes, or in the central regions of massive ones. However, for the typical baryon fractions of Λ CDM

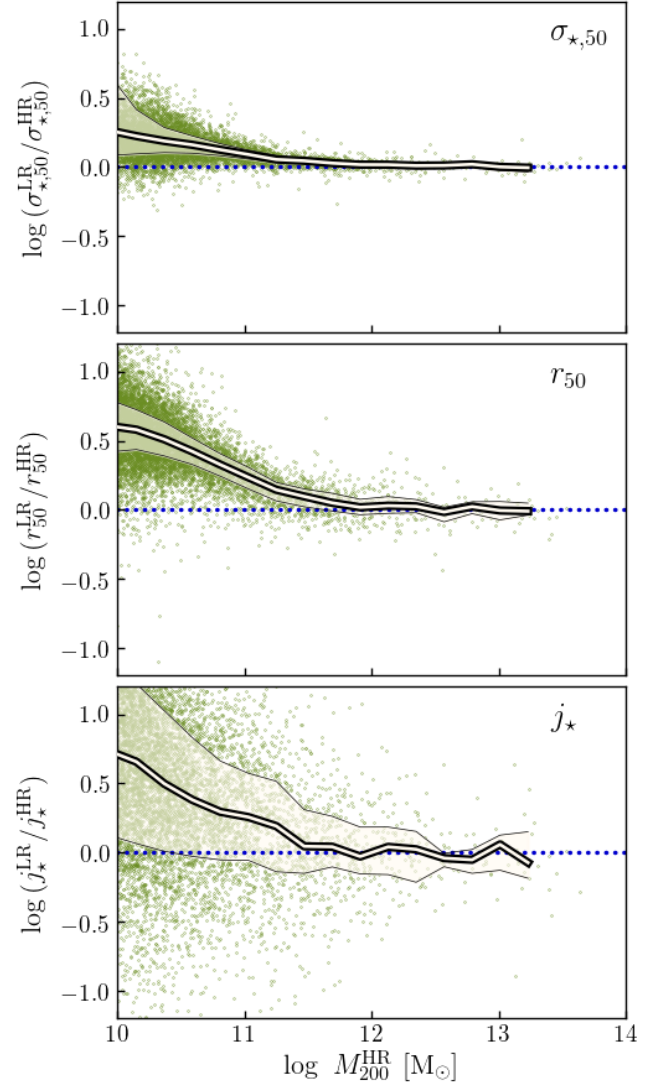


Figure 4. Logarithmic difference between the characteristic velocity dispersion ($\sigma_{*,50}$; top panel), half-mass radius (r_{50} ; middle panel), and specific angular momentum (j_* ; bottom panel) of central galaxies that were cross-matched between our simulations; results are plotted as a function of M_{200}^{HR} . As in Fig. 1, individual galaxies are shown using green points, the median relations using thick grey lines (bounded by black lines), and the interquartile scatter using lightly shaded regions. Above a halo mass of $\approx a \text{ few} \times 10^{11} M_{\odot}$, these structural and kinematic quantities are largely unbiased and exhibit small scatter between the runs. Below that mass, however, all three quantities exhibit increased scatter and become increasingly biased toward higher values in LoResDM, suggesting that spurious heating leads to an increase in the velocity dispersion, size, and angular momentum of low-mass galaxies.

haloes and for standard cooling functions, this type of heating only becomes important in simulations that adopt DM particle masses $m_{\text{DM}} \gtrsim 10^9 M_{\odot}$, which is much larger than the values used for our runs.

3.3 The stellar-halo and stellar-black hole mass relations

The good agreement between the stellar and black hole masses of central galaxies apparent in Fig. 1 has implications for a number of important statistics of the galaxy population, e.g. the stellar-halo and stellar-black hole mass relations. Because of their importance as diagnostics for subgrid model calibration, we plot these relations explicitly in Fig. 3, using solid and dashed lines to differentiate the median relations obtained for central and satellite galaxies, respectively (note that M_{200} and M_{sub} define the total halo masses of central and satellites, respectively).

The median $M_{\star} - M_{\text{halo}}$ relations (upper panel) closely overlap at all stellar masses plotted (i.e. $M_{\star} \gtrsim 10^7 M_{\odot}$, which is roughly equivalent to the mass of 5 primordial baryonic particles). The horizontal offset between the relations obtained for centrals and satellites is largely due to tidal stripping, which reduces the halo masses of satellite galaxies more readily than their stellar masses (e.g. Fattahi et al. 2018). The dots, which show individual central galaxies, suggest that the scatter in the relations are also similar, not surprising given the strong correlation between the stellar masses of individual galaxies plotted in Fig. 1 (for clarity, individual satellites are not shown). The dashed green line shows the best-fitting double power-law⁹ to the $M_{\star} - M_{200}$ relation of centrals.

In the bottom panel we plot the stellar mass-black hole mass relations obtained from our simulations. The solid circles show individual central galaxies and the open circles individual satellites. As with the stellar-to-halo mass relation, the stellar-black hole mass relations are in excellent agreement.

As a corollary of these results, the galaxy stellar mass functions, and the mass functions of gaseous baryons, central black holes, and dark matter haloes are also well converged in our runs, typically agreeing to better than 10 per cent at all mass scales plotted in the figures above. This applies to the full galaxy population, but also separately to central and satellite galaxies (see Appendix A).

4 GALAXY PROPERTIES THAT ARE AFFECTED BY SPURIOUS HEATING

The results presented in the previous section suggest that the star formation rates and baryonic masses of cross-matched galaxies are similar in our runs, with no systematic differences between them. We have also verified that the spatial and density distributions of the star forming gas particles that they contain are also similar. Any differences in the structure or kinematics of stellar particles within haloes long after their formation must therefore arise from subsequent processes. This justifies using our simulations to study the effects of spurious heating on stellar motions in simulated galaxies. We explore this below.

4.1 Characteristic stellar velocities, sizes and angular momenta

Fig. 4 shows the logarithmic difference between the two simulations for the characteristic velocity dispersion ($\sigma_{\star,50}$; top panel), stellar half-mass radius (r_{50} ; middle column), and specific angular momentum (j_{\star} ; bottom panel) of matched centrals. We use plotting conventions familiar from Fig. 1. This figure highlights one of our main results, namely that the kinematic and structural properties of galaxies

⁹ The double power-law model is $M_{\star}/M_{\text{halo}} = A[(M_{\text{halo}}/M_0)^{-\beta} + (M_{\text{halo}}/M_0)^{\gamma}]^{-1}$, with parameter values $A = 0.0702$, $M_0 = 10^{11.59} M_{\odot}$, $\beta = 1.376$, and $\gamma = 0.608$.

– particularly low-mass ones – are affected by spurious heating.¹⁰ At a halo mass of $M_{200} \approx 10^{11} M_{\odot}$, for example, $\sigma_{\star,50}$ is on average ≈ 30 per cent higher for galaxies in LoResDM than for those in HiResDM, despite them having similar baryonic and total masses (this bias is larger than the interquartile halo-to-halo scatter at this mass, shown as lightly shaded regions in each panel of Fig. 1). Although this kinematic bias diminishes with increasing mass, at the mass resolution of EAGLE it is noticeable for $M_{200} \lesssim 10^{12} M_{\odot}$ (corresponding to $M_{\star} \lesssim 10^{10} M_{\odot}$); for $M_{200} \gtrsim 10^{12} M_{\odot}$, however, the bias has diminished considerably (for quantities measured at r_{50} , but the bias is present at smaller radii; see Appendix B2).

As discussed by Ludlow et al. (2019a), the increased velocity dispersion that arises due to spurious heating leads to artificial size growth. This can be seen in the middle panel of Fig. 4. At $M_{200} \approx 10^{11} M_{\odot}$, the average value of r_{50} is nearly a factor of 2 larger for galaxies in LoResDM than for those in HiResDM. As for $\sigma_{\star,50}$, the bias decreases with increasing mass, but is present for many galaxies with $M_{200} \lesssim 10^{12} M_{\odot}$.¹¹

The spurious size growth, combined with the increased characteristic velocities of stellar particles, leads to an artificial increase in the specific angular momentum of low-mass galaxies, as seen in the bottom panel of Fig. 4. This implies that, at sufficiently low mass, galaxies tend to *gain* angular momentum from their surrounding DM haloes, which counters the findings of Wilkinson et al. (2023, see also Governato et al. 2004), who showed that thin galactic discs in idealised simulations tend to *lose* angular momentum to the halo as a result of spurious heating. The angular momentum of galaxies in cosmological simulations therefore exhibits a more complex dependence on spurious heating than what is captured by simple idealised simulations of secular discs. The difference between our results and those of Wilkinson et al. (2023) is partly because our cosmological runs have a high prevalence of spheroidal galaxies (their results were based on the response of isolated discs to spurious heating, which is different from that of dispersion supported spheroids), and partly due to the much larger spurious size growth of galaxies in our cosmological runs.

These results have implications for simulated galaxy scaling relations, which we investigate below. Because these relations also depend on galaxy morphology, we will consider them separately for disc galaxies (i.e. $\kappa_{\text{co}} \geq 0.35$), ellipticals (i.e. $\kappa_{\text{co}} \leq 0.25$), and for the entire galaxy population. First, however, we consider differences in the abundance of discs brought about by spurious heating.

4.2 The fraction of galactic discs

Wilkinson et al. (2023) showed that spurious heating of simulated galactic discs affects not only the kinematics of their stellar particles, but also their morphologies: discs become thicker as ordered rotational motions are converted into random motions. In Fig. 5 we plot the fraction of central galaxies that are discs as a function of their host halo virial mass, M_{200} . Discs are defined as galaxies whose

¹⁰ This implicitly assumes that, at fixed M_{200} , galaxies in HiResDM are substantially less affected by spurious heating than those in LoResDM.

¹¹ The quoted virial mass of $M_{200} \approx 10^{12} M_{\odot}$ above which the sizes and velocity dispersions of galaxies in LoResDM appear unbiased relative to those in HiResDM seems conservative based on a visual impression of Fig. 4. The bias in all three relations, though noticeable, is indeed quite small even at $M_{200} \approx 10^{11.5} M_{\odot}$. In Section 5.3 we provide a quantitative estimate of the halo mass above which spurious collisional effects at r_{50} are unimportant, which for our LoResDM run is $M_{200} \approx 10^{11.7} M_{\odot}$.

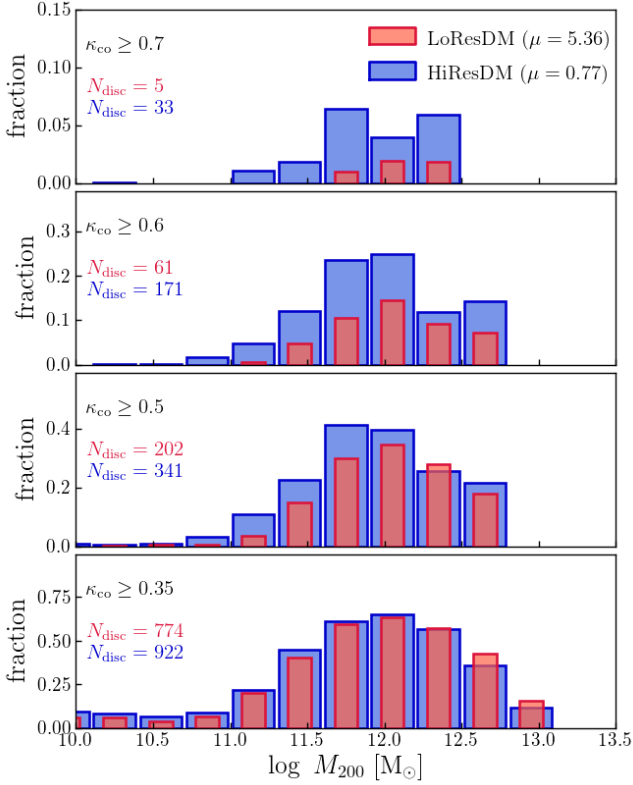


Figure 5. Fraction of central galaxies that are discs as a function of halo virial mass, M_{200} . From the bottom to top panel, discs are defined based on increasing κ_{co} thresholds, ranging from $\kappa_{\text{co}} \geq 0.35$ (bottom panel) to $\kappa_{\text{co}} \geq 0.7$ (top panel). The orange histograms show disc fractions in the LoResDM run and blue histograms show those in HiResDM. Note that the number of disc galaxies (which is quoted in each panel) is larger in HiResDM than in LoResDM, regardless of the κ_{co} threshold used. For galaxies with $\kappa_{\text{co}} \geq 0.5$, for which at least half of the stellar kinetic energy is in co-rotation, there are roughly 70 per cent more discs in HiResDM than in LoResDM.

κ_{co} values exceed a series of thresholds that increase from the bottom to the top panel. Note that in both simulations the total number of discs decreases with increasing κ_{co} , but the *fraction* of discs identified in HiResDM increases relative to that in LoResDM: e.g., for $\kappa_{\text{co}} \geq 0.5$, there are ≈ 70 per cent more discs in HiResDM than in LoResDM; for $\kappa_{\text{co}} \geq 0.7$, there are almost a factor of 7 more.

The impact of spurious heating on the morphologies of galaxies in cosmological simulations deserves a careful analysis, which we defer to future work. In the sections that follow, however, we compare several standard galaxy scaling relations obtained separately for discs (i.e. $\kappa_{\text{co}} \geq 0.35$), ellipticals (i.e. $\kappa_{\text{co}} \leq 0.25$), and for the entire galaxy populations.

4.3 Implications for galaxy scaling relations

4.3.1 The $\sigma_{*,50} - M_*$ relation

In Fig. 6 we plot the characteristic velocity dispersion of central galaxies $\sigma_{*,50}$ as a function of their stellar mass, which serves as a proxy for the Faber-Jackson (1976) relation.¹² Orange and blue

lines show the median relations for galaxies in LoResDM and HiResDM, respectively; dots of the corresponding colour show individual galaxies in the two runs. From left to right, different panels show results for the entire galaxy sample, and for the subsets of discs and ellipticals, respectively. As expected, low-mass galaxies ($M_* \lesssim 10^{10} M_\odot$) in LoResDM are kinematically hotter than the ones in HiResDM, and the discrepancy increases with decreasing stellar mass, regardless of the galactic morphology. Above a characteristic mass of $M_* \sim 10^{10} M_\odot$, however, the bias disappears and the two simulations are in good agreement.

The thick lines plotted in Fig. 6 show the median relations for the subsets of galaxies whose measured velocity dispersions, $\sigma_{*,50}$, exceeds the *spurious* velocity dispersion at r_{50} , i.e. σ_{spur} , predicted for their halo mass using the analytic model of Ludlow et al. (2021, with updates from Wilkinson et al. 2023), and were obtained as described in Section 5.3. The median relations for these galaxies are in excellent agreement.

4.3.2 The $V_{c,50} - M_*$ relation

As for the stellar velocity dispersion, the rotational velocities of galaxies – approximated here as the total circular velocity at r_{50} , i.e. $V_{c,50}$ – are also affected by the mass resolution of the DM component. Fig. 7 plots the relation between $V_{c,50}$ and M_* , a proxy for the Tully-Fisher (1977) relation, for our entire sample of central galaxies (left panel), as well as for late- (middle panel) and early-types (right panel), using the same plotting conventions as in Fig. 6.

Like their velocity dispersions, the rotation velocities of low-mass galaxies differ systematically between the runs: those in LoResDM typically have higher $V_{c,50}$ values than those in HiResDM, but the discrepancy disappears for massive, well-resolved galaxies. Indeed, thick lines in Fig. 7 show the median relations for the same subsets of galaxies used for Fig. 6, i.e. the those whose velocity dispersion exceeds the *spurious* velocity dispersion predicted for their halo mass (see Section 5.3). Regardless of morphological type, galaxies confined to these samples have unbiased rotational velocities. The systematic difference in the $V_{c,50}$ values of low-mass galaxies is partly due to their larger characteristic radii, r_{50} (see Fig. 4), which probe the rising part of the $V_c(r)$ profiles, but also due to systematic differences in their inner stellar and DM mass profiles. We briefly discuss the latter point in Section 5.2.

4.3.3 The $r_{50} - M_*$ relation

The size-mass relations obtained for central galaxies are plotted in Fig. 8. Regardless of morphological type, the two relations agree at high stellar masses (i.e. $M_* \gtrsim 10^{10} M_\odot$), but toward low masses the median curves veer away from one another, where the median sizes of galaxies in LoResDM approach a constant value of $r_{50} \approx 3.5$ kpc while those in HiResDM continue to decline. These results confirm and extend those previously obtained by Ludlow et al. (2019a).

It is tempting to associate the plateauing sizes of low-mass galaxies in LoResDM with the gravitational softening length (ϵ_{sp} is indicated by arrows in Fig. 8). However, sizes in HiResDM – which employed the *same* softening length as LoResDM – decline monotonically with decreasing mass, reaching values that are considerably smaller than $\epsilon_{\text{sp}} = 2.8 \times \epsilon$. The gravitational softening length therefore does not artificially increase the sizes of low-mass galaxies

¹² Traditionally, the Faber-Jackson (1976) relation is a projection of the fundamental plane of elliptical galaxies relating their central stellar velocity dis-

person to their total luminosity. In our analysis, $\sigma_{*,50}$ includes contributions from both the random and ordered motions of stellar particles in galaxies.

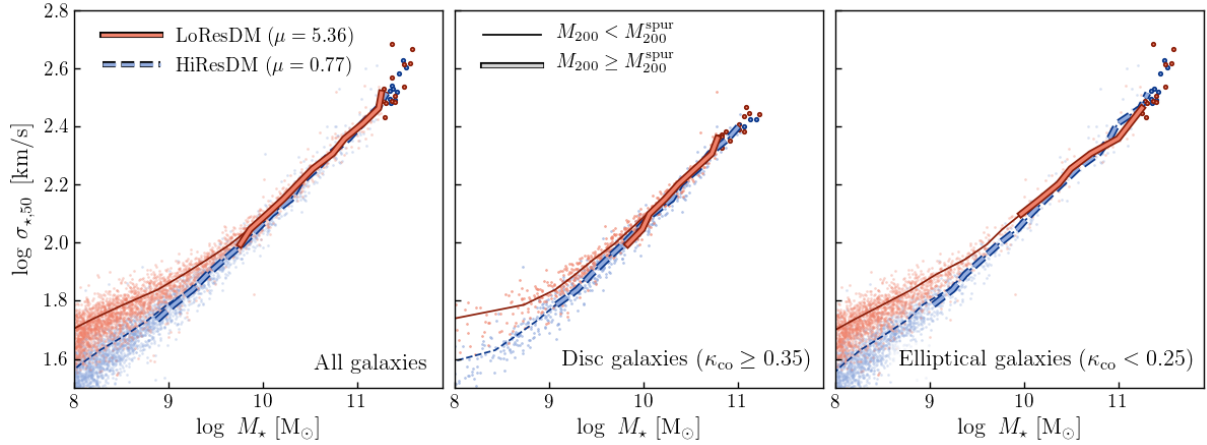


Figure 6. Total stellar velocity dispersion, $\sigma_{*,50}$ (measured within an annular aperture of central radius $R = r_{50}$), of central galaxies plotted as a function of their stellar mass, M_* . From left to right, different panels show results for the entire galaxy sample, and separately for disc ($\kappa_{\text{co}} \geq 0.35$) and elliptical galaxies ($\kappa_{\text{co}} < 0.25$), respectively. Thin coloured lines show the median relations obtained for all galaxies plotted in each panel (the individuals are shown as coloured dots); the thick lines show the median relations for the subsets of galaxies whose *measured* velocity dispersion, on average, exceeds the *spurious* velocity dispersion predicted for their halo mass using the empirical model of Ludlow et al. (2021, see Section 5.3 for details). As discussed by Ludlow et al. (2021), stellar particles in low-mass galaxies are vulnerable to spurious heating, which artificially increases their velocity dispersion.

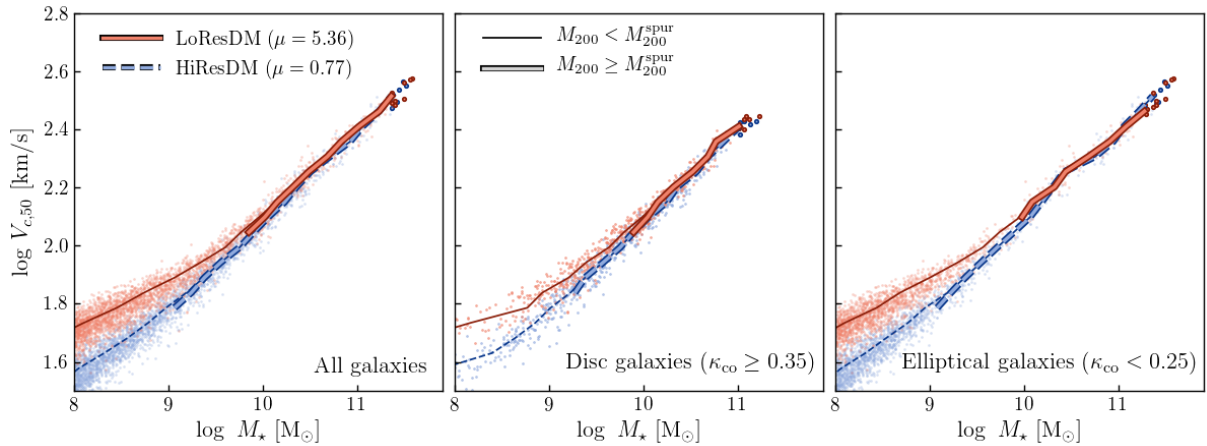


Figure 7. Same as Fig. 6, but for the rotational velocities of central galaxies (defined as the total circular velocity at the half-mass radius, r_{50} , i.e. $V_{c,50} \equiv V_c(r_{50})$). Colours, points, line styles and thicknesses have the same meaning as in Fig. 6.

in our runs,¹³ suggesting that other effects are at work. Our explanation, already emphasised by Ludlow et al. (2019a, see also Revaz & Jablonka 2018), is that spurious heating results in artificial size growth.

Support for our interpretation is provided by the thick lines in Fig. 8, which show the median size-mass relations obtained for the subset of galaxies whose velocity dispersions, $\sigma_{*,50}$, exceed the spurious velocity dispersion at r_{50} expected for their halo mass (see Section 5.3). In addition to their characteristic velocities, $\sigma_{*,50}$ and $V_{c,50}$, our empirical model offers a simple way to identify galaxies whose characteristic sizes are absolved of spurious collisional effects.

Finally, note that the median size-mass relation in HiResDM (and the relation for well-resolved galaxies in LoResDM) are accurately

approximated by the simple empirical relation¹⁴

$$r_{50} = 0.22 \times r_s, \quad (3)$$

where r_s is the NFW scale radius of the DM halo hosting the galaxy (plotted using standard scaling laws between M_{200} and concentration, see Ludlow et al. 2016, and using our best-fitting $M_* - M_{\text{halo}}$ relation). Equation (3) is shown as a dot-dashed line in each panel of Fig. 8.

¹⁴ This is a slightly modified version of the empirical relation between the half-mass radii of galaxies and the scale radii of their DM haloes proposed by Navarro et al. (2017), namely $r_{50} = 0.2 \times r_s$. Although the origin of this relation in EAGLE is unclear, it proves useful when modelling the spurious heating rates for our simulated galaxy populations, as described in Section 5.3. We acknowledge, however, that the size-mass relation of discs differs from that of spheroids in both simulations (e.g. Rodriguez-Gomez et al. 2022) and observations (Huang et al. 2017).

¹³ Ludlow et al. (2020) showed that the gravitational softening length ϵ does, in fact, affect sizes of galaxies; at fixed m_{DM} and m_{gas} , small values of ϵ exacerbate 2-body scattering, leading to systematically larger galaxy sizes, while large values of ϵ suppress the effect.

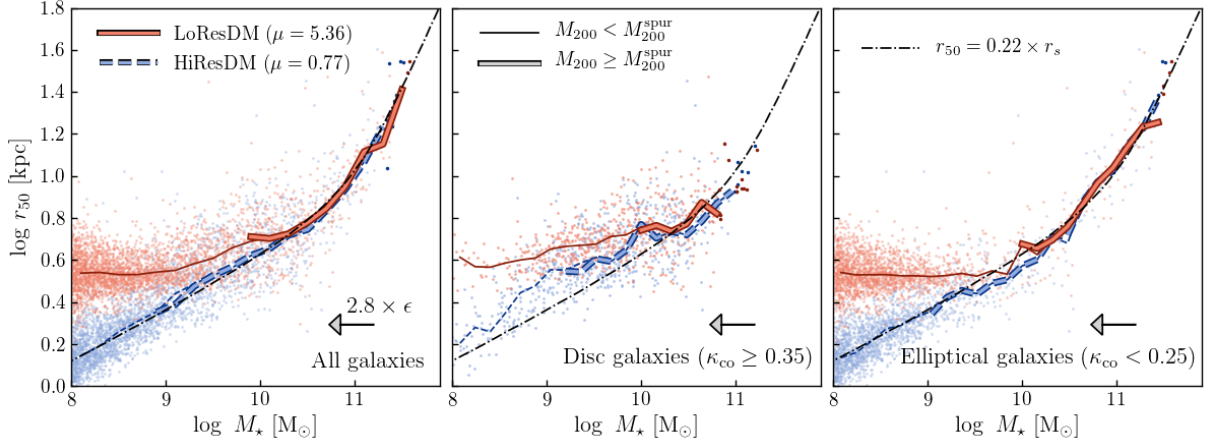


Figure 8. Size-mass relations for all central galaxies (left panel), and for the subset of disc ($\kappa_{\text{co}} \geq 0.35$; middle panel) and elliptical galaxies ($\kappa_{\text{co}} \leq 0.25$; right panel). Sizes are quantified by the three-dimensional half-stellar mass radius, r_{50} . As discussed by Ludlow et al. (2019a), low-mass galaxies are vulnerable to collisional heating and experience spurious size growth. Good convergence is obtained for systems in which spurious heating is sub-dominant (the thick lines; see Section 5.3 for details). The dot-dashed black lines in each panel show the empirical relation $r_{50} = 0.22 \times r_s$, where r_s is the scale radius of an NFW halo of virial mass M_{200} that hosts a galaxy of mass M_* inferred from the best-fitting $M_* - M_{200}$ relation plotted in Fig. 3 (we use the $r_s - M_{200}$ relation of Ludlow et al. 2016). The spline softening length, i.e. $\epsilon_{\text{sp}} \approx 2.8 \times \epsilon = 1.96 \text{ kpc}$, is shown using a grey arrow in each panel.

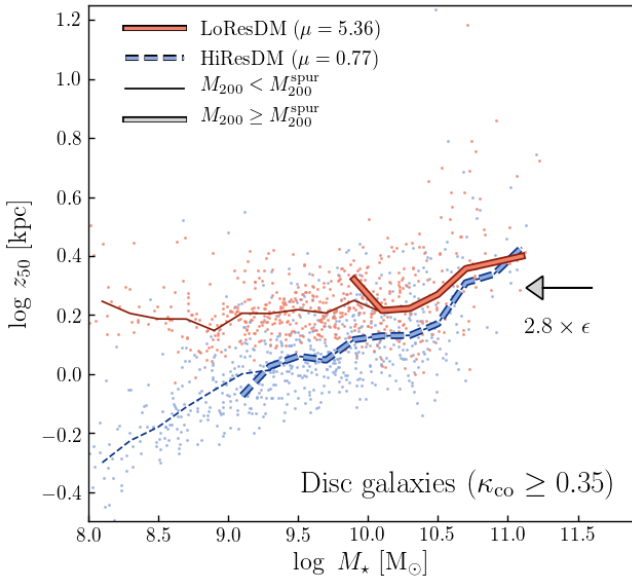


Figure 9. Vertical half-stellar mass height, z_{50} (measured within a cylindrical annulus of central radius $R = r_{50}$ and width $\Delta \log R = 0.3$), for disc galaxies ($\kappa_{\text{co}} \geq 0.35$) plotted as a function of stellar mass. Colours and line styles/weights have the same meaning as in Fig. 8.

4.3.4 The $z_{50} - M_*$ relation

The stellar half-mass heights, z_{50} , for the subset of disc galaxies, are plotted in Fig. 9 (using the same conventions as Fig. 8). As for the other structural and kinematic properties of galaxies, the scale heights of massive galaxies ($M_* \gtrsim 10^{10} M_{\odot}$) in our two simulations are in best agreement, whereas towards low masses the agreement worsens: for $M_* \lesssim 10^{10} M_{\odot}$, the half-mass heights in LoResDM are approximately constant ($z_{50} \approx \epsilon_{\text{sp}} \approx 2 \text{ kpc}$), whereas galaxies in HiResDM become progressively thinner relative to the softening length. As for r_{50} , good (though not perfect) agreement in the scale

heights of discs is obtained for those deemed unaffected by spurious heating. The median relations for these galaxies are highlighted in Fig. 9 using thick lines.

4.3.5 The $j_* - M_*$ relation

The final kinematic scaling relation we consider is the Fall (1983) relation between specific angular momentum and stellar mass, which we plot in Fig. 10. Plotting conventions (e.g. line styles, weights, and colours) and layout were inherited from previous figures.

As shown in Fig. 4, the specific angular momentum of massive galaxies in our runs are in good agreement, whereas at low masses the angular momentum of galaxies in LoResDM typically exceeds that of galaxies in HiResDM. Although idealised discs lose angular momentum to their surrounding DM haloes as a result of gravitational scattering (e.g. Governato et al. 2004; Wilkinson et al. 2023), their stellar particles tend to gain energy by the same process, which propels them onto higher energy orbits, increasing the characteristic velocity and size of the galaxy. The latter effect also occurs in dispersion supported systems, which dominate the low-mass galaxy population in our cosmological runs, increasing their angular momentum. As a result, low-mass galaxies in LoResDM have systematically *more* angular momentum than those in HiResDM with the same stellar mass.

These compensating effects reduce the galaxy mass scale above which the $j_* - M_*$ relations in our runs agree with one another. The thin and thick lines in Fig. 10 have the same meaning as in the previous two plots and show, respectively, the median relations for the entire samples of galaxies and for the subsets whose velocity dispersions, $\sigma_{*,50}$, are predicted to be free from spurious heating. Note that the $j_* - M_*$ relations for the subsets of disc and elliptical galaxies do not depend on the DM mass resolution for stellar masses $M_* \gtrsim 10^9 M_{\odot}$ (corresponding to halo masses $M_{200} \gtrsim 10^{11.1} M_{\odot}$).

Finally, note that the difference in the angular momentum of low-mass galaxies that arises due to spurious heating is much smaller than the intrinsic difference in the angular momentum content of discs and spheroids, as inferred from both simulations and observations. The observed relations are shown in Fig. 10 as green lines, and

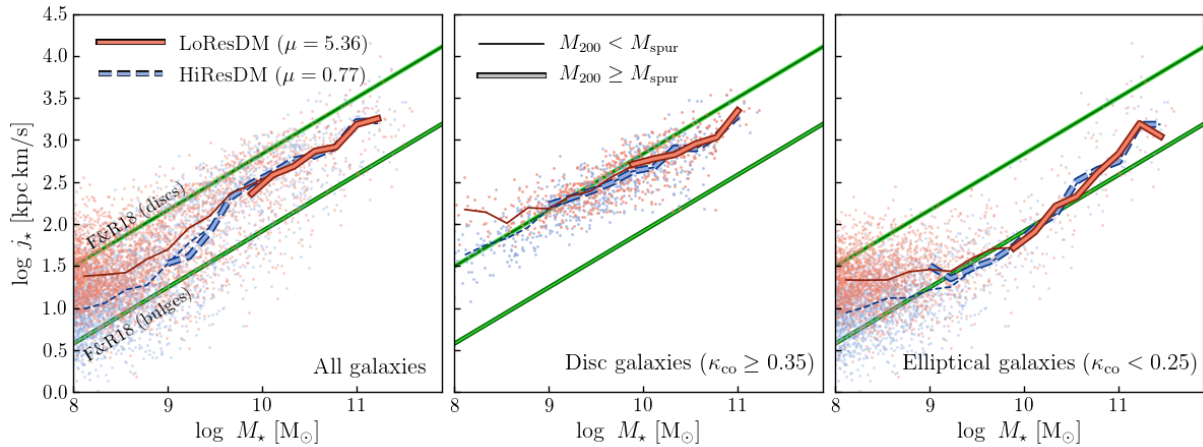


Figure 10. Total specific angular momentum as a function of stellar mass (both quantities were calculated using all stellar particles bound to each central galaxy). The different panels show results for the full galaxy population (left), and for the subset of disc (middle; $\kappa_{\text{co}} \geq 0.35$) and elliptical galaxies (right; $\kappa_{\text{co}} \leq 0.25$). The solid green lines in each panel show the relations obtained by Fall & Romanowsky (2018) for observed discs and bulges. Other plotting conventions follow from Fig. 6.

correspond to the best-fitting relations for discs and bulges obtained by Fall & Romanowsky (2018). These relations differ at all masses by about an order of magnitude, whereas the median angular momentum of $M_* \lesssim 10^9 M_\odot$ galaxies in our two simulations differ by much less (with even better agreement at higher stellar masses).

5 IMPLICATIONS OF SPURIOUS HEATING FOR COSMOLOGICAL SIMULATIONS OF GALAXY FORMATION

5.1 General considerations

In simulations of galaxy formation gas particles experience radiative energy losses and condense in the inner regions of DM haloes. Under the right conditions, stellar particles form from these gas particles, inheriting their kinematics and their masses. The baryonic components of galaxies are thus initially colder than their surrounding DM haloes.

Gravitational scattering leads to energy exchanges between DM and baryonic particles and a tendency toward energy equipartition. When $\mu > 1$, the lighter stellar particles heat up and the heavier DM particles cool down as energy exchanges strive to equalise their mean kinetic energies. This form of heating occurs even when the lighter and heavier particles are initially well mixed, and it leads to mass segregation.

Another form of heating occurs because stellar particles are initially colder than the DM. This effect is different from mass segregation: it occurs for *all* $\mu \geq 1$. For the particular case $\mu = 1$, the rate of heating by this mechanism depends on the relaxation time and hence the total number of particles by which a galaxy is resolved (i.e. at fixed mass, it depends on m_{DM}). But the maximum amount of heating is dictated by the amount of dissipation the baryons experienced. If the dissipation is large, the spurious heating can also be large, but if the dissipation is negligible, then the spurious heating will also be negligible.

The common situation in galaxy formation simulations has both energy dissipation in the baryons and differences in stellar and DM particle masses ($\mu \approx 5$), thus leading to a more complicated situation in which the rate of spurious heating depends on both particle masses

(i.e. on m_{DM} and μ), and on the amount of gaseous dissipation (i.e. on the initial separation of DM and stellar particles in phasespace). Although both effects heat stellar particles and cool DM particles, in practice we find that spurious heating is dominated by the amount of dissipation, even when $\mu > 1$. This explains the weak μ -dependence of disc heating rates reported by Ludlow et al. (2021).

We must acknowledge that the internal structure and kinematics of all galaxies in cosmological simulations are affected by spurious heating, and it is likely that the properties of their DM haloes are as well, at least in their centres. In the sections that follow, we show that this is indeed the case and offer some guidance on how to disentangle spurious results from robust ones.

5.2 Resolving the inner structure of galaxies and their dark matter haloes

Assessing numerical convergence in hydrodynamical simulations is complex, particularly when the spatial scales relevant for feedback from stars and AGN are not resolved, as is usually the case. Defining samples of “well-resolved” galaxies is therefore difficult and rarely done convincingly. For example, past studies using EAGLE have adopted different lower limits on galaxy stellar masses ($M_{*,\text{lim}}$, above which results are *assumed* to be robust), even when carrying out similar analyses. Some have adopted $M_{*,\text{lim}} \approx 10^9 M_\odot$ (e.g. Furlong et al. 2017; Ferrero et al. 2017, corresponding to several hundred stellar particles), while others used $M_{*,\text{lim}} \approx 10^{10} M_\odot$ (corresponding to several thousand stellar particles, e.g. Correa et al. 2017; Ferrero et al. 2021; de Graaff et al. 2022); others chose values in between (e.g. Lagos et al. 2017; van de Sande, et al 2019; Thob et al 2019). For IllustrisTNG-100, which has a mass and spatial resolution comparable to that of EAGLE, the situation is similar.

Motivated by this, in Fig. 11 we plot radial profiles of the average circular velocity (upper panels) and velocity dispersion (lower panels) for galaxies with $M_* \approx 10^9 M_\odot$, $10^{9.5} M_\odot$, and $10^{10} M_\odot$, which roughly span the range of $M_{*,\text{lim}}$ values mentioned above (left to right panels, respectively; note that we use a bin width of $\Delta \log M_* = 0.3$). The profiles are plotted separately for DM (grey curves), stellar (yellow curves) and gas particles (blue curves; for gas particles we plot the velocity dispersion perpendicular to the disc plane), using solid lines for LoResDM and dashed lines for

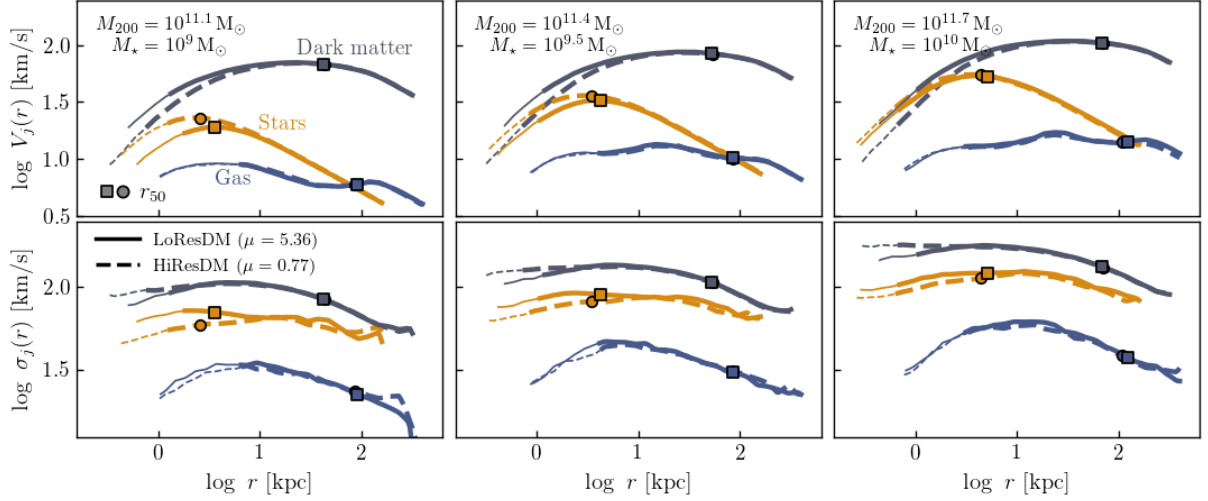


Figure 11. Top panels plot the contribution to the total circular velocity profile due to dark matter (dark grey curves), stellar (yellow curves) and gas particles (blue curves); bottom panels plot velocity dispersion profiles of each component (for gas particles, we plot the one-dimensional velocity dispersion perpendicular to the plane of the gaseous disc, which is the component most susceptible to spurious heating). From left-to-right, the three columns correspond to galaxies (and their DM haloes) with different stellar masses: $M_* = 10^9 M_\odot$, $10^{9.5} M_\odot$, and $10^{10} M_\odot$, respectively. The corresponding average halo masses, M_{200} , are also indicated, and do not differ between the two runs. In all panels, results from LoResDM and HiResDM are plotted using solid and dashed lines, respectively, with thin (thick) lines extending to the smallest radii enclosing 10 (100) particles of each species. Circles or squares marked along each curve indicate the location of the half-mass radius of each component. The values of stellar mass chosen for this plot are comparable to the lower mass limits imposed by various authors on the analysis of simulations with mass and force resolution comparable to ours (see text for details).

HiResDM. The thick and thin lines are plotted to minimum radii that enclose, on average, 100 and 10 particles of each type, respectively; the half-mass radii are indicated by symbols along each curve (squares for LoResDM; circles for HiResDM). These profiles clarify the results reported in previous sections, and highlight several others.

First, the radial profiles for gas closely overlap at all radii, even when only ≈ 10 particles are enclosed. Artificial heating of gas particles by DM particles is therefore unimportant in our simulations (but likely is important for simulations that use very massive DM particles; e.g. Steinmetz & White 1997). For gas particles, radiative cooling dissipates the energy gained by spurious heating, which explains why the *global* properties of galaxies in our runs (e.g. the total baryonic masses, SFHs, etc.) are in good agreement, even when the internal structure and kinematics of their stellar components are not.

There is also good agreement between the *outer* $V_j(r)$ and $\sigma_j(r)$ profiles for stellar and DM particles. However, systematic differences are evident at small radii that become more apparent toward low masses. Specifically, galaxies in LoResDM have more extended and kinematically hotter stellar components, but more concentrated and (slightly) cooler central DM distributions.¹⁵ Note that differences in the $V_*(r)$ and $\sigma_*(r)$ profiles at fixed mass extend to radii that exceed r_{50} , suggesting that differences in the $\sigma_{*,50} - M_*$ and $V_{c,50} - M_*$ relations obtained from our simulations (Figs. 6 and 7, respectively) are not merely due to differences in the radius r_{50} at which these characteristic velocities were measured.

Note too that the results plotted in Fig. 11 differ from the expectations of simple adiabatic contraction models, which predict that more compact galaxies give rise to higher central DM densities. Our results, in fact, show the opposite trend, and one that is consistent

with the expectations of spurious heating. As discussed by Ludlow et al. (2019a, see also Ludlow et al. 2020), energy is more readily transferred from DM to stellar particles by 2-body scattering when $\mu \gtrsim 1$, and the net effect is for galaxies to heat-up and expand, while DM haloes cool down and contract (i.e. σ_{DM} decreases at fixed r and V_{DM} increases at fixed r). This effect is apparent in all panels of Figure 11. Unless great care is taken to eliminate galaxies affected by spurious heating, cosmological simulations should therefore not be used to develop or calibrate empirical models for the baryon-induced contraction of DM haloes.

Finally, note that for all mass bins plotted in Figure 11, the circular velocity profiles of DM haloes are *not converged* at radii $r \lesssim r_{50}$ (i.e. below the stellar half-mass radius), even when their stellar and gaseous $V_c(r)$ profiles are converged. This has important implications for modelling the rotation curves and DM fractions of the least-massive galaxies in hydrodynamical simulations, which are also sensitive to spurious heating. Models for predicting the “convergence radius” of DM haloes, such as those advocated by Power et al. (2003) and Ludlow et al. (2019b), will require revision to accommodate these results.

5.3 A convergence criterion for spurious heating in cosmological hydrodynamical simulations

Ludlow et al. (2021, and later Wilkinson et al. 2023) derived and tested a useful approximation for the evolution of σ_i (the three cylindrical components of the stellar velocity dispersion, i.e. σ_R , σ_ϕ , and σ_z) that arises due to the spurious heating of simulated galactic discs by DM halo particles. This model is

$$\sigma_i^2 = \sigma_{\text{DM}}^2 - (\sigma_{\text{DM}}^2 - \sigma_{i,0}^2) \times \exp\left(-\frac{t}{t_{\sigma_i}}\right), \quad (4)$$

¹⁵ Differences in the concentrations of the stellar or DM distributions shown in Fig. 11 can be inferred by comparing their circular velocities at fixed radii: higher/lower $V_j(r)$ implies a higher/lower concentration.

Table 2. Values of M_{200}^{spur} at $z = 0$ required for convergence in galactic structure and kinematics at the half stellar mass radius, r_{50} , for various cosmological simulations. The values for HiResDM were estimated using the median $\sigma_{*,50} - M_{200}$ relation in that run (see Fig. 12), and are provided for several values of the DM particle mass. The value obtained for the 100 (25) cubic Mpc EAGLE run is provided in the row labelled EAGLE-100 (EAGLE-25); rows labelled TNG-100 and TNG-50 provide the M_{200}^{spur} values for the IllustrisTNG-100 and IllustrisTNG-50 simulations, respectively.

Sim.	$N_{\text{DM}}/N_{\text{gas}}$	m_{DM} [$10^5 M_{\odot}$]	μ $m_{\text{DM}}/m_{\text{gas}}$	M_{200}^{spur} [$10^{10} M_{\odot}$]	N_{200}^{spur} [10^4]
HiResDM	1	97.0	5.36	54.9	5.7
HiResDM	2	48.5	2.68	36.2	7.5
HiResDM	3	32.3	1.79	28.1	8.7
HiResDM	4	24.2	1.34	23.7	10.0
HiResDM	5	19.4	1.07	20.7	10.6
HiResDM	6	16.2	0.89	18.5	11.4
HiResDM	7	13.9	0.77	16.8	12.1
EAGLE-100	1	97.0	5.36	54.9	5.1
EAGLE-25	1	12.2	5.36	9.91	8.2
TNG-100	1	75.0	5.36	50.1	9.9
TNG-50	1	4.50	5.36	7.9	26.1

where

$$t_{\sigma_i} = \frac{V_{200}^3}{G^2 \rho_{\text{DM}} m_{\text{DM}}} \left[\sqrt{2} \pi k_i \ln \Lambda \left(\frac{\rho_{\text{DM}}}{\rho_{200}} \right)^{\alpha_i} \left(\frac{V_{200}}{\sigma_{\text{DM}}} \right)^2 \right]^{-1} \quad (5)$$

is a characteristic ‘‘heating’’ timescale at which $\sigma_i \sim \sigma_{\text{DM}}$ (the local 1-dimensional velocity dispersion of DM), and $\sigma_{i,0}$ is the initial velocity dispersion in the i direction.¹⁶

For $\sigma_{i,0} \ll \sigma_i \ll \sigma_{\text{DM}}$, equation (4) reproduces the disc heating rates derived analytically by Lacey & Ostriker (1985). But for $t \gg t_{\sigma_i}$, σ_i approaches σ_{DM} , which reproduces the results of idealised simulations of poorly-resolved galactic discs on timescales of order or less than the ages of galaxies of interest ($t \lesssim 10$ Gyr).

The total spurious velocity dispersion predicted by equation (4) is given by

$$\sigma_{\text{spur}}^2 = \sum_i \sigma_i^2 = \sigma_{\text{R}}^2 + \sigma_{\phi}^2 + \sigma_z^2, \quad (6)$$

and depends on halo mass through V_{200} , and on galacto-centric radius through σ_{DM} and ρ_{DM} . The latter, ρ_{DM} , is fully specified by the cosmological parameters (see e.g. Ludlow et al. 2016; López-Cano et al. 2022) and σ_{DM} can be obtained from Jeans’ equations, allowing predictions to be made for the level of spurious heating a simulated galaxy may have undergone given its age and halo mass.¹⁷

In Fig. 12, we compare the predictions of equation (4) for the total spurious stellar velocity dispersion (dot-dashed lines) to the values of $\sigma_{*,50}$, measured in our simulations. Both dispersions are

¹⁶ Equation (4) above, which is equivalent to equation (6) in Wilkinson et al. (2023), is motivated by the disc heating rates derived analytically by Lacey & Ostriker (1985). In their case, the parameters $\alpha_i = 0$ and $k_i \ln \Lambda$ in equation (5) can be calculated explicitly when a velocity distribution for DM particles is specified. In this paper, we adopt the parameter values listed in Table 2 of Wilkinson et al. (2023), i.e. $(\alpha_{\text{R}}, \alpha_z, \alpha_{\phi}) = (-0.189, -0.308, -0.115)$ and $(k_{\text{R}}, k_z, k_{\phi}) \ln \Lambda = (20.17, 20.19, 9.40)$. We refer the interested reader to Ludlow et al. (2021) and Wilkinson et al. (2023) for a detailed discussion of our disc heating model.

¹⁷ A python script to calculate the spurious disc heating rate based on equation (4) can be found at <https://github.com/AaronDLudlow/hot-disc.git>.

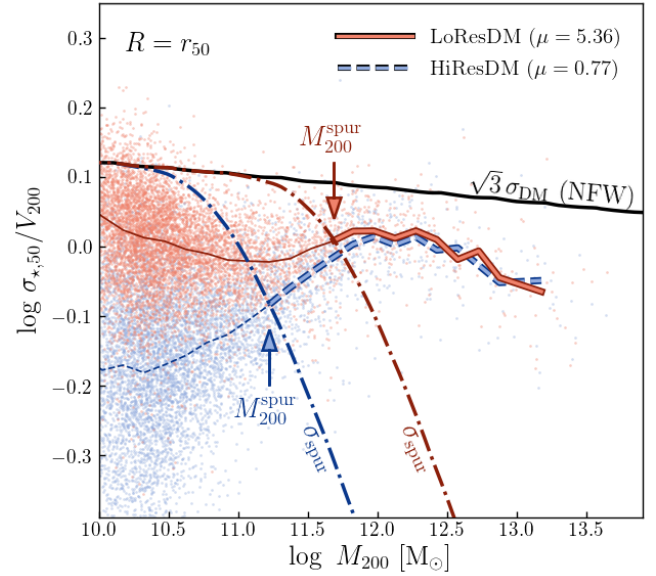


Figure 12. Stellar velocity dispersion $\sigma_{*,50}$ at r_{50} for central galaxies plotted as a function M_{200} (and normalised by V_{200}). Orange and blue colours distinguish our LoResDM and HiResDM runs, respectively. The solid black line shows the total DM velocity dispersion at r_{50} for an isotropic NFW halo (assuming $r_{50} = 0.22 \times r_s$ where r_s is the halo scale radius; see Fig. 8). The two dot-dashed lines labelled σ_{spur} show the spurious velocity dispersion predicted for our runs using equation (4), assuming a galaxy age of $t_* = 7.6$ Gyr (approximately the median half-mass stellar age of galaxies with $M_* \geq 10^9 M_{\odot}$). Individual galaxies are shown as small dots and the median relations as coloured lines. The arrows labelled M_{200}^{spur} indicate the halo masses at which σ_{spur} intersects the median velocity dispersion-stellar mass relation of galaxies in each simulation. These median relations are shown using thick and thin lines, respectively, for $M_{200} \geq M_{200}^{\text{spur}}$ and $M_{200} \leq M_{200}^{\text{spur}}$.

normalised by V_{200} and are plotted as a function of M_{200} . Note that our model assumes $\sigma_{i,0} = 0$ and a stellar half-mass radius of $r_{50} = 0.22 \times r_s$ (see Fig. 8; r_s was obtained from the mass-concentration relation of Ludlow et al. 2016), and we adopt a typical age $t = 7.6$ Gyr, roughly the median half-mass age of EAGLE galaxies with $M_* \geq 10^9 M_{\odot}$.

The $\sigma_{*,50} - M_{200}$ relations from our simulations evoke trends seen in previous figures; above a characteristic halo mass they coincide, but below that mass they differ.¹⁸ Importantly, this characteristic halo mass roughly coincides with the mass above which the median velocity dispersion of the galaxies in LoResDM first exceeds the *spurious* velocity dispersion σ_{spur} predicted by equation (4).¹⁹ This halo mass is labelled M_{200}^{spur} in Fig. 12 and is pinpointed by coloured arrows (orange for LoResDM and blue for HiResDM). For both simulations, the median $\sigma_{*,50} - M_{200}$ relations are represented

¹⁸ Note that the lowest-mass galaxies plotted in Fig. 12 are not maximally heated, as anticipated by equation (4). This may be because 1) their stars are not mono-age (younger stars are less affected by spurious heating than older ones); or 2) the effects of spurious heating are suppressed by the gravitational force softening, which is only slightly smaller than the half-mass radii of the lowest mass galaxies (see, e.g., Ludlow et al. 2019a).

¹⁹ We have verified that similar results are obtained when this comparison is limited to any of the three orthogonal components of the velocity dispersion, i.e. σ_{R} , σ_z , and σ_{ϕ} .

by thick line segments for $M_{200} \geq M_{200}^{\text{spur}}$, where they are in good agreement. At M_{200}^{spur} , the median relations differ by ≈ 0.03 dex.

Other fundamental properties of galaxies occupying haloes with masses $M_{200} \geq M_{200}^{\text{spur}}$ are also converged, specifically those plotted in Figs. 6 through 9, where we also used thick and thin lines to distinguish the median relations for galaxies with $M_{200} \geq M_{200}^{\text{spur}}$ and $M_{200} < M_{200}^{\text{spur}}$, respectively. Fig. 12 therefore summarises our main result: *the kinematic and structural properties of galaxies are robust to spurious heating provided the intrinsic velocity dispersion of their stellar particles exceeds the spurious velocity dispersion predicted by equation (4).*

Although the velocity dispersions plotted in Fig. 12 were measured at r_{50} , we show in Appendix B that equation (4) can also be used to assess whether spurious heating is important at other galactocentric radii and for mono-age stellar populations, for which different levels of heating are expected.

6 SUMMARY

We have used two cosmological, smoothed-particle hydrodynamical simulations based on the EAGLE model of galaxy formation to study the impact of spurious heating of stellar particles by DM particles on the properties of simulated galaxies. Our simulations differ only in the mass of their DM particles (those in HiResDM are a factor of 7 less massive than those in LoResDM), but share all other numerical and subgrid parameters, including the baryonic particle mass and force resolution. The main features of the simulations are described in Section 2 and Table 1. Our main results are summarised below.

(i) In Section 3 we identified several global properties of the galaxy population that are not affected by spurious collisional heating: their total stellar, gas, and black hole (BH) masses, and the virial masses of their dark matter (DM) haloes (Fig. 1). When matched between the runs, the stellar and gas masses of individual galaxies do, however, exhibit non-negligible scatter that increases with decreasing halo mass. This is usually attributed to the stochastic star formation and feedback models often adopted for cosmological simulations (e.g. Borrow et al. 2022), but may also arise from the spurious numerical effects discussed in this paper. The scatter for BH masses, decreases with decreasing halo mass. This is because the majority of low-mass haloes ($M_{200} \lesssim 10^{11} M_{\odot}$) contain only one central BH particle, whose mass is a small multiple of the BH seed mass. The virial masses of individual haloes typically agree to better than 10 per cent. The good agreement between the baryonic masses of galaxies stems from similarities in their star formation histories (Fig. 2).

(ii) As a result, both simulations have similar stellar-halo and stellar-BH mass relations (Fig. 3), as well as similar stellar, BH, and DM halo mass functions (for both central and satellite galaxies; Fig. A1). Once the subgrid parameter values have been chosen for a simulation such that it reproduces observations of the galaxy stellar mass function, or the observed relation between stellar and BH masses, they should therefore not require re-calibration if the DM mass resolution is increased such that $\mu \approx 1$.

(iii) In Section 4 we showed that the structural and kinematic properties of the stellar components of simulated galaxies are affected by spurious collisional heating. For example, the fraction of disc galaxies (whose κ_{co} values exceed various thresholds) is higher in HiResDM than in LoResDM (Fig. 5), in qualitative agreement with predictions of Wilkinson et al. (2023). Spurious heating also artificially increases the stellar velocity dispersion (Fig. 6), rotation velocity (Fig. 7), size (Fig. 8), thickness (Fig. 9), and angular momentum (Fig. 10) of low-mass galaxies; in all cases, the bias be-

tween LoResDM and HiResDM increases with decreasing mass. The structural and kinematic properties of the gaseous components of galaxies are not affected by spurious collisional heating, at least for the DM particle masses we study in this paper.

(iv) As a result, spurious collisional heating changes the normalisation and slope of simulated galaxy scaling relations, unless efforts are made to eliminate systems that have been adversely affected by it. The Faber-Jackson (1976) relation between velocity dispersion and stellar mass (Fig. 6), the Tully-Fisher (1977) relation between rotation velocity and stellar mass (Fig. 7), and the Fall (1983) relation between angular momentum and stellar mass (Fig. 10) are all sensitive to spurious heating, as are structural relations between galaxy scale radius, scale height, and stellar mass (Figs. 8 and 9).

(v) Gravitational scattering transfers energy from DM halo particles to stellar particles (when $\mu \geq 1$), causing galaxies to heat-up and expand, while haloes cool-down and contract (Fig. 11). As a result, galaxies in HiResDM are more baryon dominated than those in LoResDM; the latter have higher DM fractions in their inner regions. This result opposes the naive expectations of virtually all models for the baryon-induced contraction of DM haloes, and has important implications for modelling the DM fractions of galaxies using cosmological simulations.

(vi) Fortunately, the structural and kinematic properties of galaxies at various characteristic radii are robust to spurious heating provided they occupy haloes above a resolution-dependent virial mass, M_{200}^{spur} . For the 100 cubic Mpc flagship run of the EAGLE project (and our LoResDM run, both of which have $m_{\text{DM}} = 9.7 \times 10^6 M_{\odot}$), and for quantities measured at the stellar half-mass radius, r_{50} , this corresponds to $M_{200} \gtrsim M_{200}^{\text{spur}} = 10^{11.7} M_{\odot}$ (or $N_{200} \gtrsim 5.1 \times 10^4$). This coincides with the halo mass above which the *intrinsic* velocity dispersion of central galaxies in LoResDM (i.e. the values of $\sigma_{*,50}$ measured directly from the simulated particle data) exceeds the *spurious* velocity dispersion predicted by the empirical disc heating model of Ludlow et al. (2021, see Fig. 12). Equation (4) therefore provides a simple but accurate convergence criterion that can be used to identify and eliminate galaxies whose structure and kinematics are influenced by numerical heating (see Section 5.3 for details). Suppressing spurious heating at smaller/larger radii than r_{50} , or for old/young stellar populations, requires haloes to be resolved with more/fewer DM particles (see Appendix B).

Our study highlights the potential harms of spurious collisional heating for the results of cosmological simulations of galaxy formation, and provides a simple but effective method to identify galaxies whose structural and kinematic properties are most likely to be at risk. Based on our analysis, we expect that galaxies in the 100 cubic Mpc-volume simulation of the EAGLE project (Schaye et al. 2015; Crain et al. 2015, which has a DM particle mass of $m_{\text{DM}} = 9.7 \times 10^6 M_{\odot}$) occupying DM haloes with masses less than $M_{200}^{\text{spur}} \lesssim 10^{11.7} M_{\odot}$ (or $M_{*} \lesssim 10^{10} M_{\odot}$) are negatively affected by spurious heating, and should not be considered in future analyses of galaxy structure or kinematics.

We can use our model to make predictions for the values of M_{200}^{spur} relevant for other cosmological simulations. For our HiResDM run, we predict spurious collisional heating to be negligible at r_{50} for galaxies occupying haloes with $M_{200} \gtrsim M_{200}^{\text{spur}} = 10^{11.2} M_{\odot}$ (corresponding to $N_{200} \gtrsim 1.2 \times 10^5$). For the 25 cubic Mpc high-resolution run of the EAGLE project (for which $m_{\text{DM}} = 1.21 \times 10^6 M_{\odot}$) we find $M_{200}^{\text{spur}} \approx 10^{11.0} M_{\odot}$ (or $N_{200}^{\text{spur}} \approx 8.2 \times 10^4$). Similarly, for IllustrisTNG-100 we find $M_{200}^{\text{spur}} \approx 10^{11.7} M_{\odot}$ ($N_{200}^{\text{spur}} \approx 9.9 \times 10^4$).

and for IllustrisTNG-50 (Pillepich et al. 2019) we obtain²⁰ $M_{200}^{\text{spur}} \approx 10^{10.9} M_{\odot}$ ($N_{200}^{\text{spur}} \approx 2.6 \times 10^5$). Note that, to within a factor of a few, and for this specific set of cosmological simulations, $N_{200}^{\text{spur}} \sim 10^5$ (although different values of N_{200}^{spur} will be required to suppress spurious heating at other galacto-centric radii).

Table 2 lists these values of M_{200}^{spur} , as well as a few additional values for our HiResDM run that assume different relative numbers of DM and baryonic particles (i.e. different DM particle masses at fixed baryonic particle mass). Note that the values of M_{200}^{spur} obtained for EAGLE and IllustrisTNG exceed the lower limits on halo masses (or the corresponding limits on stellar masses) often adopted for the analysis of these runs.

Although our analysis focused mainly on the stellar component of central galaxies at $z = 0$, it can be extended to explore the redshift dependence of spurious heating, its impact on the kinematics and structure of satellite galaxies, its effect on galaxy morphology or on the radial profiles of stellar velocity dispersion or circular velocity. Spurious heating will also affect the fine structure of simulated galaxies, including the abundance of bars, spiral arms, and stellar age or metallicity gradients. We plan to investigate these topics in future work.

Future cosmological simulations of galaxy formation would benefit from being run with higher resolution in the DM component than what is traditionally used. The optimal value of μ is likely to be decided by separate considerations about baryon and DM mass resolutions, where m_{gas} is chosen so that the sub-grid recipes for star formation and feedback yield sensible galaxy populations and m_{DM} is chosen so that the rate of spurious heating is reduced to tolerable levels. The additional computational cost for the latter alone will be less than that required to increase the DM and baryonic mass resolutions together. This will smooth the DM potential on small scales, thereby reducing the impact of spurious heating and allowing galaxies with lower baryonic masses to be resolved. Because its effects are primarily restricted to low masses, the impact of spurious heating on galaxies in existing or future large-volume simulations can be quantified using smaller volume simulations that vary μ but not the baryonic particle mass or subgrid model parameters.

Our simulations adopted the same softening length for both resolutions (and for baryonic and DM particles). The softening length is known to modify the effects of spurious collisional heating, suppressing it for large values, but enhancing it for small values (Ludlow et al. 2020). Future simulations may also profit from being carried out with optimally-chosen or adaptive softening lengths for collisionless particles (e.g. Hopkins et al. 2023) to further suppress the insidious effects of spurious collisional heating.

We hope our work stimulates others to reconsider the validity of results from existing simulations and to make deliberate efforts to improve the reliability of future simulations.

ACKNOWLEDGEMENTS

We thank Adrian Jenkins and Sylvia Ploekinger for helpful conversations. ADL and DO acknowledge financial support from the Australian Research Council through their Future Fellowship scheme (project numbers FT160100250, FT190100083, respectively). This work benefited from the following public PYTHON packages: SCIPY

(Virtanen et al. 2020), NUMPY (Harris et al. 2020), MATPLOTLIB (Hunter 2007) and IPYTHON (Pérez & Granger 2007).

DATA AVAILABILITY

Our simulation data can be made available upon reasonable request. Our Theoretical results can be reproduced from the equations provided in Section 5.3. A python script to calculate the spurious disc heating rate based on equation (4) can be found at <https://github.com/AaronDLudlow/hot-disc.git>.

REFERENCES

- Abazajian K. N., et al., 2009, *ApJS*, 182, 543
 Borrow J., Schaller M., Bahe Y. M., Schaye J., Ludlow A. D., Ploekinger S., Nobels F. S. J., Altamura E., 2022, arXiv e-prints, p. arXiv:2211.08442
 Correa C. A., Schaye J., 2020, *MNRAS*, 499, 3578
 Correa C. A., Schaye J., Clauwens B., Bower R. G., Crain R. A., Schaller M., Theuns T., Thob A. C. R., 2017, *MNRAS*, 472, L45
 Crain R. A., et al., 2015, *MNRAS*, 450, 1937
 Faber S. M., Jackson R. E., 1976, *ApJ*, 204, 668
 Fall S. M., 1983, in Athanassoula E., ed., Vol. 100, *Internal Kinematics and Dynamics of Galaxies*. pp 391–398
 Fall S. M., Romanowsky A. J., 2018, *ApJ*, 868, 133
 Fattahi A., Navarro J. F., Frenk C. S., Oman K. A., Sawala T., Schaller M., 2018, *MNRAS*, 476, 3816
 Ferrero I., et al., 2017, *MNRAS*, 464, 4736
 Ferrero I., Navarro J. F., Abadi M. G., Benavides J. A., Mast D., 2021, *A&A*, 648, A124
 Furlong M., et al., 2017, *MNRAS*, 465, 722
 Genel S., et al., 2019, *ApJ*, 871, 21
 Governato F., et al., 2004, *ApJ*, 607, 688
 Harris C. R., et al., 2020, *Nature*, 585, 357–362
 Hernquist L., Barnes J. E., 1990, *ApJ*, 349, 562
 Hopkins P. F., Nadler E. O., Grudić M. Y., Shen X., Sands I., Jiang F., 2023, *MNRAS*,
 Huang K.-H., et al., 2017, *ApJ*, 838, 6
 Hunter J. D., 2007, *Computing in Science & Engineering*, 9, 90
 Keller B. W., Wadsley J. W., Wang L., Kruijssen J. M. D., 2019, *MNRAS*, 482, 2244
 Lacey C. G., Ostriker J. P., 1985, *ApJ*, 299, 633
 Lagos C. d. P., Theuns T., Stevens A. R. H., Cortese L., Padilla N. D., Davis T. A., Contreras S., Croton D., 2017, *MNRAS*, 464, 3850
 López-Cano D., Angulo R. E., Ludlow A. D., Zennaro M., Contreras S., Chaves-Montero J., Aricò G., 2022, *MNRAS*, 517, 2000
 Ludlow A. D., Bose S., Angulo R. E., Wang L., Hellwing W. A., Navarro J. F., Cole S., Frenk C. S., 2016, *MNRAS*, 460, 1214
 Ludlow A. D., Schaye J., Schaller M., Richings J., 2019a, *MNRAS*, 488, L123
 Ludlow A. D., Schaye J., Bower R., 2019b, *MNRAS*, 488, 3663
 Ludlow A. D., Schaye J., Schaller M., Bower R., 2020, *MNRAS*, 493, 2926
 Ludlow A. D., Fall S. M., Schaye J., Obreschkow D., 2021, *MNRAS*, 508, 5114
 Navarro J. F., Benítez-Llambay A., Fattahi A., Frenk C. S., Ludlow A. D., Oman K. A., Schaller M., Theuns T., 2017, *MNRAS*, 471, 1841
 Pérez F., Granger B. E., 2007, *Computing in Science and Engineering*, 9, 21
 Pillepich A., et al., 2018, *MNRAS*, 473, 4077
 Pillepich A., et al., 2019, *MNRAS*, 490, 3196
 Planck Collaboration et al., 2014, *A&A*, 571, A16
 Power C., Navarro J. F., Jenkins A., Frenk C. S., White S. D. M., Springel V., Stadel J., Quinn T., 2003, *MNRAS*, 338, 14
 Revaz Y., Jablonka P., 2018, *A&A*, 616, A96
 Richings J., Frenk C., Jenkins A., Robertson A., Schaller M., 2021, *MNRAS*, 501, 4657
 Rodriguez-Gomez V., et al., 2022, *MNRAS*, 512, 5978

²⁰ To obtain these values, we adopt a size-mass relation appropriate for well-resolved galaxies in IllustrisTNG; specifically, $r_{50} = 0.15 \times r_s$.

- Sales L. V., Navarro J. F., Schaye J., Dalla Vecchia C., Springel V., Booth C. M., 2010, MNRAS, 409, 1541
 Schaye et al. 2015, MNRAS, 446, 521
 Sellwood J. A., 2013, ApJ, 769, L24
 Sellwood J. A., 2015, MNRAS, 453, 2919
 Springel V., 2005, MNRAS, 364, 1105
 Springel V., White S. D. M., Tormen G., Kauffmann G., 2001, MNRAS, 328, 726
 Steinmetz M., White S. D. M., 1997, MNRAS, 288, 545
 Thob et al 2019, MNRAS, 485, 972
 Tully R. B., Fisher J. R., 1977, A&A, 54, 661
 Virtanen P., et al., 2020, Nature Methods, 17, 261
 Wilkinson M. J., Ludlow A. D., Lagos C. d. P., Fall S. M., Schaye J., Obreschkow D., 2023, MNRAS, 519, 5942
 York D. G., et al., 2000, AJ, 120, 1579
 de Graaff A., Trayford J., Franx M., Schaller M., Schaye J., van der Wel A., 2022, MNRAS, 511, 2544
 van de Sande, et al 2019, MNRAS, 484, 869

APPENDIX A: MASS FUNCTIONS OF GALAXIES, BLACK HOLES, AND DARK MATTER HALOES

The left panel of Fig. A1 shows the galaxy stellar mass functions (GSMF) for the full galaxy population (solid lines) and for the subset of satellite galaxies (dashed lines). Orange and blue lines correspond to LoResDM and HiResDM, respectively, and extend to a limiting mass of $M_* = 9.1 \times 10^6 M_\odot$ (roughly 5 primordial gas particles). The GSMFs are in excellent agreement across the entire mass range plotted (the bumps and wiggles at high masses are due to Poisson noise).

In the middle panel of Fig. A1, we plot the mass functions for the central supermassive black holes of central (solid lines) and satellite galaxies (dashed lines). Curves are plotted to $M_{\text{BH}} = 10^{5.5} M_\odot$, roughly twice the black hole seed mass. The excellent agreement between the runs extends across the entire mass range.

The right-hand panel of Fig. A1 shows the DM halo and subhalo mass functions. We plot haloes hosting central galaxies using solid lines (their masses are defined as M_{200}); dashed lines show the subhalo mass functions (whose masses are M_{sub}). The DM halo mass functions agree remarkably well down to a halo mass equal to about 50 DM particles, which is the lowest mass plotted.

Finally, the thin dot-dashed lines in the right-hand panel of Fig. A1 show the DM halo mass functions (obtained using M_{sub}) for all DM haloes hosting luminous galaxies (i.e. those with $M_* \geq 5 \times m_{\text{gas}}$). Apart from slight discrepancies at the lowest halo masses (below about $10^9 M_\odot$, which roughly corresponds to haloes resolved by ≈ 100 DM particles in LoResDM), the curves are in excellent agreement. In both simulations, these low-mass haloes contain $\lesssim 1$ per cent of the total stellar mass, and are largely inconsequential for the total stellar mass formed in either simulation.

APPENDIX B: CONVERGENCE CRITERIA FOR SPURIOUS COLLISIONAL HEATING OF DIFFERENT STELLAR POPULATIONS AND AT DIFFERENT GALACTO-CENTRIC RADII

The spurious disc heating rate predicted by equation (4) depends on the local density and velocity dispersion of DM particles, which depend strongly on galacto-centric radius: heating rates will be higher at $r < r_{50}$, where DM densities are higher, and lower at $r > r_{50}$, where DM densities are lower. Furthermore, spurious heating is an integrated effect and also depends on the age of the galaxy or stellar

population: older galaxies (or stellar populations) will have experienced higher levels of heating than younger ones, even if they occupy DM haloes with the same mass and internal structure. Below we test our convergence criterion by applying it to galaxy properties measured at different radii, or for different mono-age stellar populations at a fixed fiducial radius.

B1 Application to mono-age stellar populations

In the upper panels of Fig. B1, we plot the velocity dispersion $\sigma_{*,50}$ (normalised by V_{200}) as a function of M_{200} for subsets of mono-age stellar particles (note: $\sigma_{*,50}$ was measured at the r_{50} value of *all* stellar particles). Orange and blue colours distinguish our LoResDM and HiResDM runs, respectively. From left-to-right, the different columns correspond to stellar populations aged between 0 to 2 Gyr, 4 to 6 Gyr, and 8 to 10 Gyr. The solid black lines show the DM halo velocity dispersion at r_{50} (where $r_{50} = 0.22 \times r_s$; see Section 5.3), and the dot-dashed coloured lines show the spurious velocity dispersion at r_{50} after $t = 1$ Gyr (left), 3 Gyr (middle), and 9 Gyr (right) as predicted by equation (4).

The values of M_{200}^{spur} (indicated by arrows in each panel of Fig. B1) provide an accurate account of the halo mass scale above which $\sigma_{*,50}$ is unaffected by spurious heating, for all ages of the stellar particles considered. We show this explicitly by plotting masses $M_{200} \geq M_{200}^{\text{spur}}$ using thick lines and $M_{200} < M_{200}^{\text{spur}}$ using thin lines.

The lower panels of Fig. B1 confirm that our convergence criterion also applies to the structure of mono-aged stellar particles. Here we plot (as a function of M_* rather than M_{200}) the half-mass radii r_{50} of each mono-aged stellar population. Thick and thin lines differentiate the same populations as in the upper panels.

B2 Application to different galacto-centric radii

In the upper panels of Fig. B2 we plot the stellar velocity dispersion $\sigma_{*,f}$ (normalised by V_{200}) at $R = r_{25}$ (left; enclosing 25 per cent of the stellar mass), $R = r_{50}$ (middle), and $R = r_{75}$ (right; enclosing 75 per cent of the stellar mass) as a function of M_{200} . The solid black lines in each panel show the DM velocity dispersion at at these radii, assuming an isotropic NFW halo. For haloes, we assume $r_{50} = 0.22 \times r_s$ (r_s is prescribed by the mass-concentration relation of Ludlow et al. 2016), and infer r_{25} and r_{75} assuming a spherical exponential profile and our best-fitting stellar-to-halo mass relation in double power-law form (see footnote 9 and Fig. 3). The values obtained this way roughly reproduce the median values of r_{25} and r_{75} measured in our simulations, as seen in the lower panels. There we plot, in the same order, the values of r_{25} , r_{50} , and r_{75} as a function of M_* , using coloured curves (and points) for the simulation results and dot-dashed black lines for the inferred r_f values.

As in Fig. B1, the dot-dashed coloured lines in the upper panels (labelled σ_{spur}) show the spurious velocity dispersion at r_f predicted by equation (4) assuming a galaxy age of $t = 7.6$ Gyr. The thick lines in the upper panels (solid for LoResDM; dashed for HiResDM) show the median $\sigma_{*,f} - M_*$ relations for galaxies with haloes of mass $M_{200} \geq M_{200}^{\text{spur}}$, and are in good agreement; the thin lines of each type, which differ significantly, correspond to galaxies in lower-mass haloes. The same subsets of galaxies are distinguished in the lower panels of Fig. B2 (i.e. using thick lines for those with $M_{200} \geq M_{200}^{\text{spur}}$ and thin lines for the rest), and show that all three characteristic sizes r_{25} , r_{50} , and r_{75} , as well as the velocity dispersions at these radii, are robust to spurious collisional heating provided $M_{200} \geq M_{200}^{\text{spur}}$.

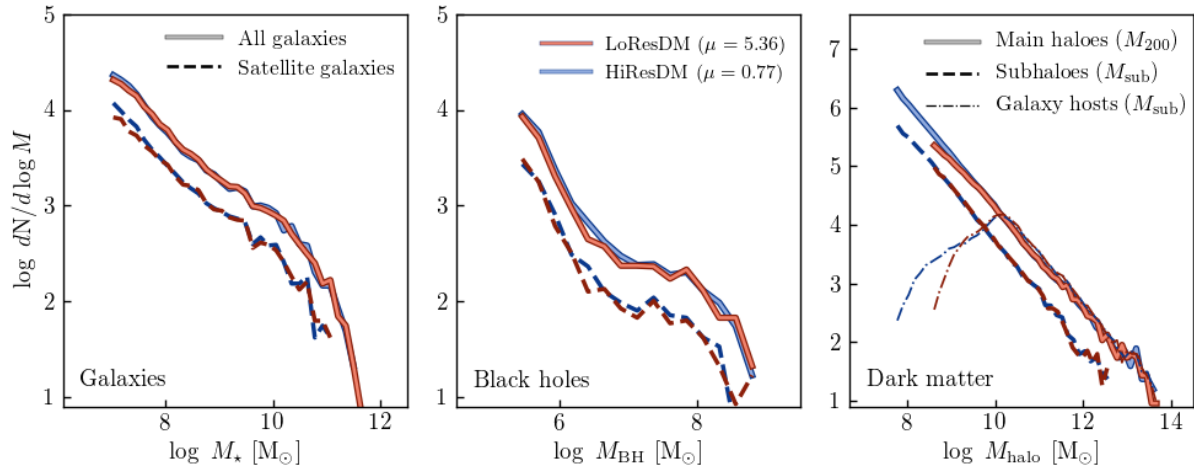


Figure A1. Mass functions for galaxies (left panel), central supermassive black holes (middle panel), and DM haloes and subhaloes (right panel). Results from LoResDM are shown using orange lines and those from HiResDM using blue lines. Stellar and central black hole mass functions are plotted for the entire population of galaxies (centrals plus satellites; solid lines), as well as for the subset of satellite galaxies (dashed lines). Dark matter halo mass functions are shown for central haloes (based on M_{200} ; solid lines), for the entire population of satellite subhaloes (dashed lines), and for the subset of (sub)haloes (which in this case includes central and satellite haloes) hosting galaxies with stellar masses $M_* \geq 5 \times m_{\text{gas}}$ (based on M_{sub} ; dot-dashed lines). DM halo mass functions are plotted to a limiting mass corresponding to 50 DM particles in each run, GSMFs are plotted above a limiting mass of 5 primordial gas particles, and black hole mass functions are plotted above $M_{\text{BH}} = 10^{5.5} M_{\odot}$, which is roughly twice their seed mass.

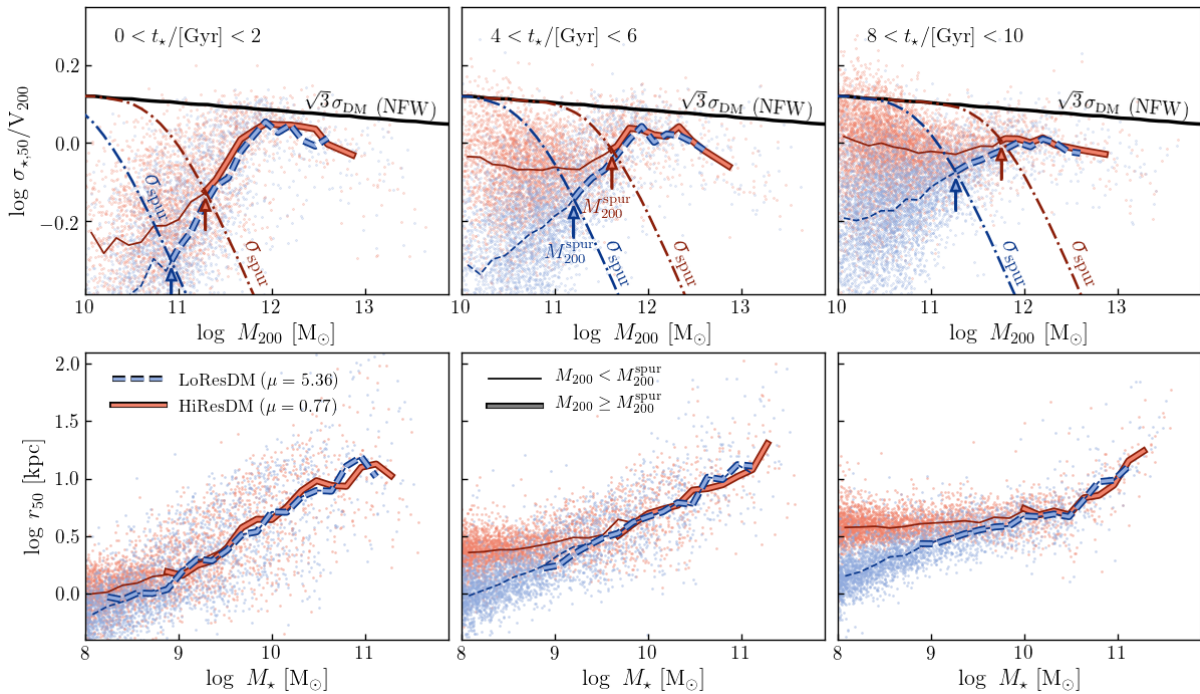


Figure B1. The importance of spurious collisional heating for mono-age stellar populations. The upper row is modelled after Fig. 12, and plots the stellar velocity dispersion-halo mass relations; the lower row, similar to Fig. 8, plots the size-mass relations. From left to right, the different columns show results for stellar populations of increasing age: $0 \leq t_*/[\text{Gyr}] \leq 2$ (left), $4 \leq t_*/[\text{Gyr}] \leq 6$ (middle) and $8 \leq t_*/[\text{Gyr}] \leq 10$ (right). The values of $\sigma_{*,50}$ are measured at the half-mass radius of *all* stars in each galaxy, not only those in each mono-age bin; the sizes correspond to the half stellar-mass radii of each mono-age population. The solid black lines in the upper panels plot the (isotropic) velocity dispersion of an NFW DM halo at r_{50} , assuming $r_{50} = 0.22 \times r_s$. The dot-dashed lines (labelled σ_{spur} in the upper panels) show the velocity dispersion at r_{50} due to spurious collisional heating after $t = 1$ Gyr (left), 5 Gyr (middle), and 9 Gyr. In all panels, thin lines show the median results for all galaxies, whereas thick lines are limited to the subset of galaxies that pass the convergence criterion outlined in Section 5.3.

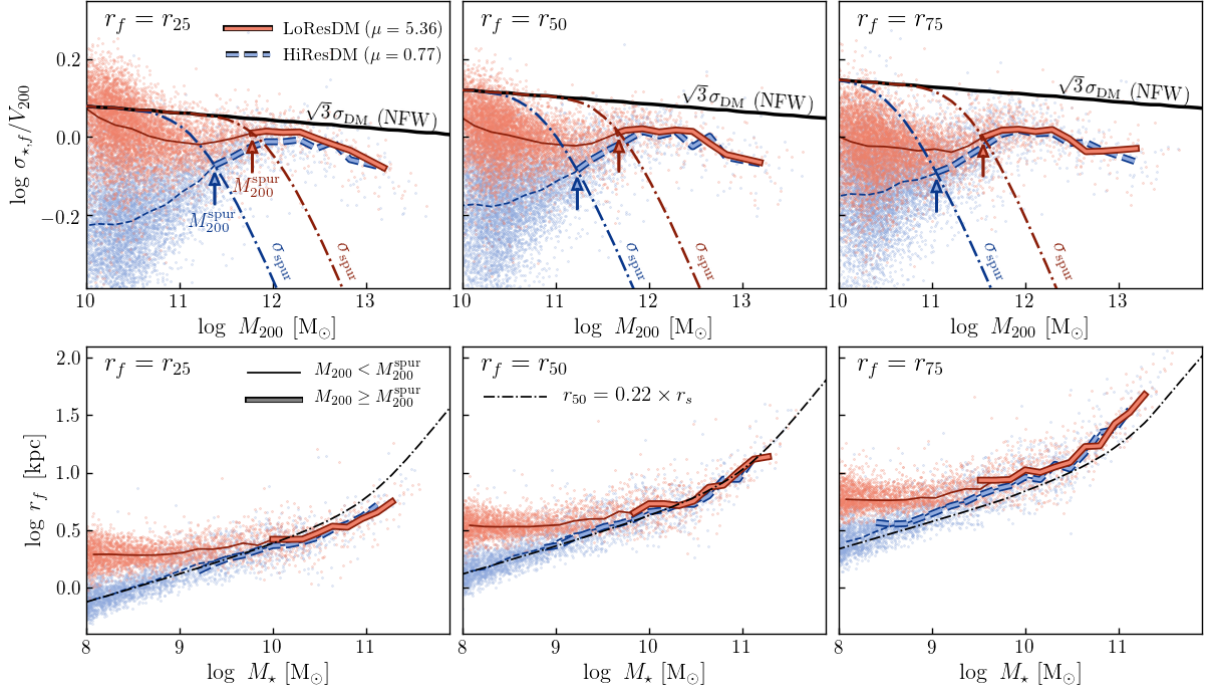


Figure B2. Same as Fig. B1 but for the galacto-centric radii r_{25} (left), r_{50} (middle) and r_{75} (right) enclosing 25, 50, and 75 per cent of the stellar mass of each galaxy. The dot-dashed lines in the lower-left and lower-right panels are empirical estimates of r_{25} and r_{75} obtained assuming $r_{50} = 0.22 \times r_s$ and a spherical exponential stellar mass profile.

This paper has been typeset from a $\text{\TeX}/\text{\LaTeX}$ file prepared by the author.